Pro Gradu

Large-Area SINIS Tunnel Junctions for Cooling Applications

Ville Valkiala

02.10.2015

DEPARTMENT OF PHYSICS
UNIVERSITY OF JYVÄSKYLÄ

Preface

The work reported in this Master's thesis has been done between June 2014 and December 2015 at Nanoscience Center at the Department of Physics in the University of Jyväskylä.

First, I would like to thank my supervisor Ilari Maasilta for giving me an opportunity to work in his research group and for providing a really interesting topic for my thesis. In addition, I would like to thank Kimmo Kinnunen for helping me with the low temperature measurements. Also, I would like to thank all current and former group members, and especially Saumyadip Chaudhuri and Geng Zhuoran.

Jyväskylä December, 2015

Ville Valkiala

Abstract

NIS tunnel junctions are small-scale structures consisting of a superconductor and a normal metal separated by a thin insulating barrier. They can be used in cooling applications at ultra low temperatures. A SINIS junction contains two NIS junctions in series. The cooling power of the device is proportional to the area of the junction and the energy gap of the superconductor ($\Delta^{1/2}$). In this work large-area Al/AlO_x/Cu junctions were fabricated with standard lithographic techniques and ultra high vacuum evaporation. The areas of the junctions are 60 μm x 60 μm and 30 μm x 30 μm. Current-voltage characteristics of the devices were measured at millikelvin temperature range using ^{3}He-^{4}He-dilution refrigerator. The obtained IV and dI/dV data deviates from ideal BCS behavior, but still shows some typical tunnel junction characteristics. In addition to aluminum, Nb/Al/AlO_x/Cu junctions with niobium as the superconducting electrode were also fabricated. Nb is the element with the highest energy gap, making it theoretically ideal material for SINIS cooler fabrication.

Tiivistelmä

Työn aiheena on pinta-alaltaan suuret SINIS-tunneliliitokset ja niiden käyttö jäähdytyksessä. SINIS-tunneliliitos koostuu kahdesta normaalimetalli-eriste-suprajohde (NIS) rakenteesta, jotka ovat kytkettynä toisiinsa sarjaankytkennällä. Tällaisia rakenteita voidaan käyttää jäähdytyksessä matalissa lämpötiloissa. Tämän mahdollistaa suprajohteille ominainen energia-aukko Δ, joka tarkoittaa, että tietyillä energian arvoilla suprajohteessa ei ole sallittuja tiloja, joille elektronit voisivat asettua. Energia-aukko sijoittuu keskitetysti Fermi-energian E_F kohtaan, joka tarkoittaa että lämpötilassa $T = 0$ kaikki Fermi-energian alapuolella olevat tilat ovat miehitettyjä ja sen yläpuolella olevat tyhjillään. Kun normaalimetallin ja suprajohteen välille kytketään jännite, metallien Fermi-tasoja voidaan muuttaa, ja elektronit pystyvät tunneloitumaan normaalimetallista suprajohteeseen. Sopivalla jännitteen arvolla vain korkeimman energian omaavat elektronit normaalimetallissa ovat energiassa suprajohteen energia-aukon yläpuolella, joten vain ne pystyvät tunneloitumaan. Tämä pienentää normaalimetallin keskimääräistä energiaa, joten sen lämpötila laskee.

SINIS-tunneliliitoksen jäähdytysteho on verrannollinen liitoksen pinta-alaan ja energia-aukon neliöjuureen. Tämän takia jäähdytystehoa saadaan teorian mukaan kasvatettua käyttämällä mahdollisimman suuria liitospinta-aloja ja suprajohdemateriaaleja, joilla on mahdollisimman suuri energia-aukko.

Tässä työssä valmistettiin 60 μm x 60 μm ja 30 μm x 30 μm Al/AlO_x/Cu SINIS liitoksia ja mitattiin niiden virta-jännite käyttäytymistä matalissa lämpötiloissa. Alumiinin lisäksi myös niobia kokeiltiin suprajohdemateriaalina, koska sillä on alkuainesuprajohteista suurin energia-aukko. Tulokset osoittavat, että valmiiden näytteiden käyttäytyminen eroaa ideaalisesta teorian mukaisesta käyttäytymisestä, mutta siinä on kuitenkin selvästi nähtävissä tyypillisiä tunneliliitoksille ominaisia piirteitä.

Contents

1 Introduction

The field of modern cryogenics was made a reality over one hundred years ago when Kamerlingh Onnes was able to liquefy helium in 1908. This opened up a whole new direction for research, since now it became possible to study properties of matter at temperatures close to absolute zero. It didn't take long to discover that some materials completely lose their electrical resistivity below a certain temperature i.e. become superconducting. This was first demonstrated in 1911. The lowest attainable temperature was soon reduced from 4.2 K of liquid helium. One of the most important steps was the invention of the dilution refrigerator in the early 1960s. It could reach temperatures below 100 mK, and nowadays there are dilution refrigerators with base temperatures of 2 mK. Even in the early days, there were techniques such as demagnetization refrigeration that could reach a lower temperature than with dilution refrigerators, but the latter has the advantages of continuous cooling and relatively large cooling power.

Tunnel junctions are devices with two electrodes separated by a narrow insulating barrier. In a NIS junction, one of the electrodes is superconducting in which case the tunneling current does not behave linearly with respect to bias voltage. This type of tunneling was first demonstrated by Giaever and Fisher [1]. They also made the first normal metal junctions using aluminum oxide as the tunneling barrier [2]. NIS junctions can be used for cooling the electronic temperature of the normal metal because of the energy gap of the superconductor. This refrigeration method was first used by Gray et al. [3], but instead of cooling they called it gap enhancement. Nahum et al. [4] introduced the modern description for NIS junctions in 1994 and used them for cooling Cu normal metal with an $Al/AlO_x/Cu$ junction. They were able to lower the electronic temperature of Cu from 100 mK to 85 mK. Two years later Leivo et al. [5] were able to improve this and they achieved cooling from 300 mK to 100 mK. This was done by using two NIS junctions symmetrically in series (SINIS). According to theory, the cooling power of a NIS junction can be increased by decreasing the tunneling resistance or increasing the energy gap of the superconductor. Tunneling resistance is lowered by using

larger junction areas, and so Clark et al. developed a method to fabricate large-area tunnel junctions [6] in 2004. However, attempts to increase the junctional area using different methods have been presented even earlier e.g. by Castle et al. [7]. Another way to increase the cooling power is to use a superconducting material with a higher energy gap than that of aluminum. Niobium has the largest transition temperature of elemental superconductors ($\approx$ 9 K) i.e. the largest energy gap. Niobium NIS junctions have been successfully fabricated here at the University of Jyväskylä [8]. Also derivatives of niobium such as NbN are used since they have even higher energy gaps than pure Nb [9].

The main advantage in using tunnel junction refrigerators is their simple design [10]. Dilution refrigeration and other methods using cryogenic liquids are quite expensive and they require lots of space and specialized equipment. That limits their use to cryogenic laboratories. Tunnel junctions are small in size and require only a small voltage to work. They can also be easily integrated into other electronics. However, they are limited by the starting temperature that must be reached until tunnel junction cooling can be utilized. That is why they are feasible only in special applications such as the final stage in a refrigerator. Another possible application is to use them to cool high energy resolution detectors in space [11].

SINIS tunnel junctions with large junction areas are studied in this work. These junctions are fabricated with electron beam lithography mostly based on a method developed by Castle et al. [7]. Superconductive electrodes are made of aluminum or niobium and the tunnel barrier oxide is always oxidized aluminum. Current-voltage characteristics of these junctions were measured at cryogenic temperatures using dilution refrigeration. Also differential conductance measurements were performed to directly measure the energy gap of the superconductor.

Large-area tunnel junction coolers have been successfully fabricated before by two research groups. Pekola's group in Aalto University [12] who were able to reach 32 mK using a pair of 40 μm x 7 μm NIS junctions and Ullom's group in NIST [13] who used several pairs of 32 μm x 7 μm NIS junctions to cool macroscopic (centimeter scale) Cu islands.

2 Theory

2.1 Superconductivity

Superconductivity is a phenomenon exhibited by certain materials, metals such as aluminum and niobium, for example. When such a material is cooled below a certain temperature known as critical temperature T_C, its electrical resistivity decreases to zero [14]. This makes it possible for current to travel in a superconductor without energy losses. Another important factor regarding superconductivity is perfect diamagnetism. Below the critical temperature all external magnetic fields are excluded from the interior of the superconductor. This is called the Meissner effect. When a superconductor is cooled below the critical temperature in the presence of a magnetic field supercurrents are induced on the surface of the superconductor. These give rise to magnetization $\vec{M}$ which completely cancels the applied field $\vec{H}$ resulting $\vec{B} = 0$ as indicated by equation

$$\vec{B} = \mu_0(\vec{H} + \vec{M}). \tag{1}$$

When the magnetic field is increased high enough, the superconductor cannot exclude the magnetic flux any more and it reverts back to its normal state. The value of magnetic field where this occurs is called the critical field H_c. The critical field is a function of temperature and has its maximum at 0 K and goes to zero at T_c. Magnetic fields higher or equal than H_c break the superconductivity and with lower fields the Meissner effect is complete within the superconductor. Superconductors exhibiting this kind of behavior are called type I. Other possibility is type II where the superconductor behaves as type I up to a magnetic field H_{c1} but in addition it has another critical field H_{c2}. In magnetic fields higher than H_{c2} type II superconductor is at its normal state, but in fields between H_{c1} and H_{c2}, it is in a vortex state which consists of both normal and superconducting regions inside the material. Elemental superconductors are mostly of type I, and alloys and oxide superconductors type II. However, niobium is a type II superconductor

despite being an element.

The first successful theory of superconductivity was introduced by F. and R. London in 1935 [15]. Their approach was phenomenological but it was able to explain the Meissner effect. The London equations are in SI-units

$$\frac{\partial \vec{J}_s}{\partial t} = \frac{n_s e^2}{m}\vec{E} \tag{2}$$

$$\vec{\nabla} \times \vec{J}_s = -\frac{n_s e^2}{m}\vec{B} \tag{3}$$

where $\vec{J}_s$ is the superconducting current density and n_s the number density of superconducting electrons. The constant on the right hand side of both equations can also be expressed as $\frac{1}{\mu_0 \lambda_L}$ where μ_0 is the permeability of vacuum and λ_L is the London penetration depth. The latter is an important property in this theory because it describes the distance a magnetic field will penetrate into a superconductor. Even though the most important properties of superconductors can be obtained from the London equations, they still do not give any indication about the underlying cause for superconductive behavior and cannot, for example, explain the energy gap present in superconductors.

The complete microscopic theory of superconductivity was published by Bardeen, Cooper and Schrieffer in 1957 [16]. This BCS theory suggests that the phenomena associated with superconductivity are the result of electrons in the material pairing up to Cooper pairs in temperatures below the transition temperature. In other words, there is an attractive interaction between electrons to overcome the repulsive Coulomb interaction. This is generated by the electron-phonon interaction. Because of its negative charge, an electron will attract positive ions in its local proximity when moving in a material. This increases positive charge density in that area in turn attracting other electrons. That creates a weak attractive interaction between two electrons.

For more accurate description one needs to consider electron scattering [17]. If an electron has a wavevector k_1 and then it scatters to state k_1' a phonon can be emitted. Another electron can absorb that phonon and

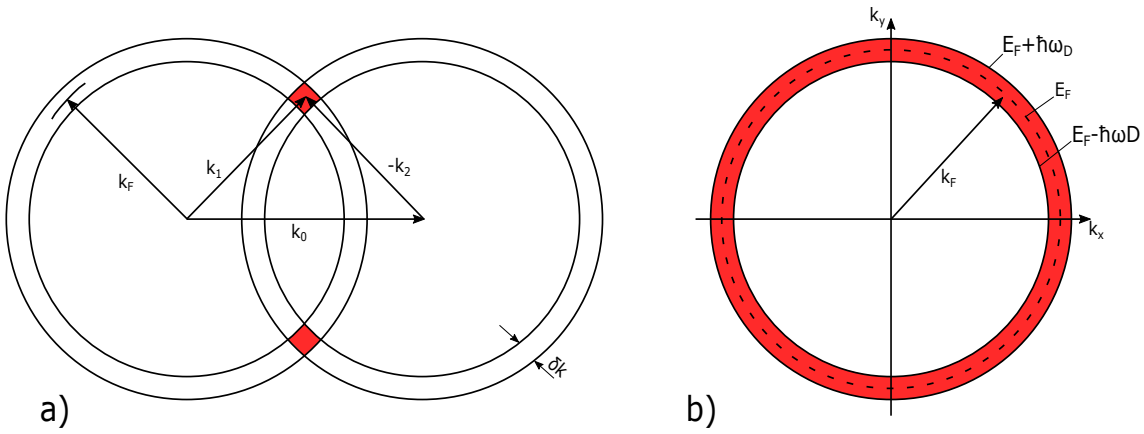

Figure 1: *Representation of the scattering process of two electrons in k-space. a) Two overlapping spherical shells of radius k_F and thickness δk fulfilling the condition $k_1 + k_2 = k_1' + k_2' = k_0$. Crystal momentum is conserved in overlapping regions of the two spheres (shown in red). b) The condition that maximizes the number of electron pairs which happens when $k_0 = 0$.*

scatter from state k_2 to k_2'. Crystal momentum must be conserved so

$$k_1 + k_2 = k_1' + k_2' = k_0. \tag{4}$$

If two electrons are added to a Fermi gas of electrons which is at 0 K, they will occupy states $E > E_F$. Scattering can be considered as two overlapping Fermi spheres in k-space separated by k_0. States capable of participation to scattering are located in a shell of thickness δk which corresponds to energies between E_F and $E_F+\hbar\omega_D$. Ω_D is the Debye frequency which is the theoretical maximum frequency of the phonon vibrations. The number of allowed states is maximized when k_0 becomes zero so in other words $k_1 = -k_2$. This is shown graphically in Fig. 1. Electron states satisfying this condition are called Cooper pairs. The attraction is caused by the phonon mediated electron-electron interaction. Above the transition temperature i.e. in the normal state the kinetic energy of the electrons is so large that it prevents the formation of permanent Cooper pairs. The spatial part of the two-electron wavefunction (Cooper pair) must be symmetric under the interchange of the two electrons because they are indistinguishable particles. Because electrons

are fermions, the total wavefunction consisting of the spatial part and the spin part must be antisymmetric to obey the Fermi-Dirac statistics, which forces the spin part to be antisymmetric. This means that the total spin $S = 0$ which corresponds to a singlet state.

2.1.1 Density of States

At absolute zero all electrons in a superconductor are bound into Cooper pairs which are in the same quantum state. In order to break a pair and excite electrons to a first excited state, energy of 2Δ is needed. This results in an energy gap Δ between the BCS ground state and the first excited single electron state. Now considering the density of states of a superconductor, there is an energy gap of 2Δ centered around the Fermi energy E_F. All the states below this energy are filled and all above it are empty. The normalized density of states near the gap can be expressed as [14]

$$n_S(E,T) = \frac{N_S(E)}{N_N(0)} = \begin{cases} \frac{|E|}{\sqrt{E^2-\Delta(T)^2}} & ,|E| > \Delta(T) \\ 0 & ,|E| < \Delta(T) \end{cases} \tag{5}$$

where $N_S(E)$ is the unnormalized density of states of a superconductor and $N_N(0)$ the density of states of a normal metal at the Fermi energy. Energy is measured from the Fermi energy so that $E_F = 0$. The energy gap is related to transition temperature by an approximate formula $\Delta \approx 1.76 k_B T_c$ in the simplest approximation in BCS theory. More accurate description for the density of states can be achieved by using the non-ideal formula by Dynes et al. [18]

$$n_S(E,T) = \left| Re\left(\frac{E + i\Gamma}{\sqrt{(E+i\Gamma)^2 - (\Delta(T))^2}} \right) \right|. \tag{6}$$

Here Γ is the Dynes parameter which can be thought to represent the non-ideality of the system. This parameter takes into account the finite lifetimes of the states, and creates states within the energy gap. The ideal case (Eq. (5)) can be obtained from this equation by setting Γ to zero. The origin of the Dynes parameter is still not well understood but it is thought to include

non-idealities as well as second order tunneling processes [19]. A theory by Pekola et al. [20] shows that the behavior described by equation (6) is caused by the influence of the electromagnetic environment of a tunnel junction, as opposed to being a property of the superconductor itself.

2.2 Tunneling

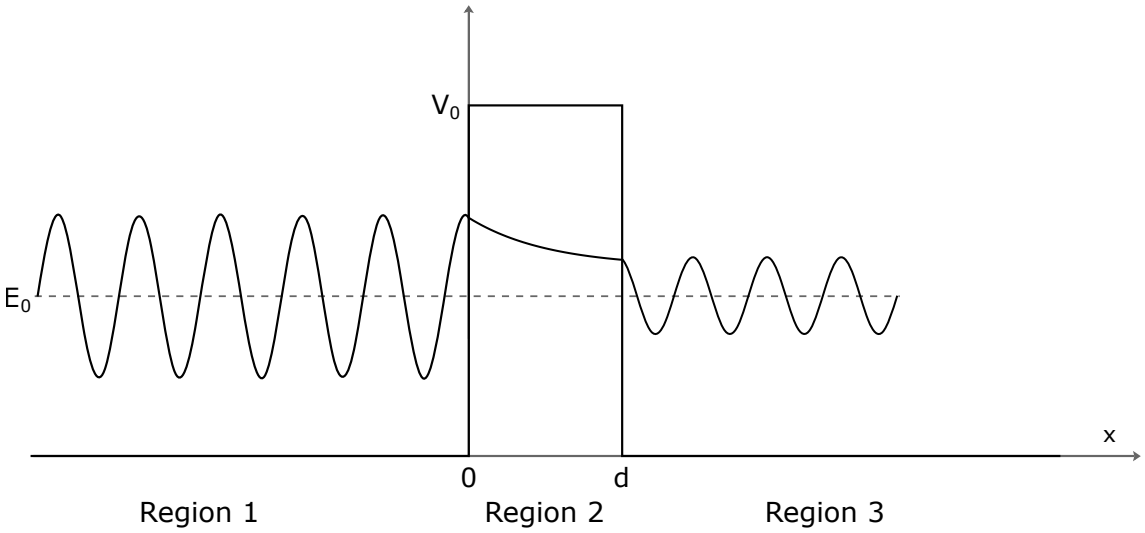

Figure 2: *One dimensional case of an electron tunneling through a potential barrier of energy V_0 located between 0 and d. Electron is coming from the left and it has an average energy of E_0. Only incident and transmitted waves are shown.*

Tunneling is a quantum mechanical phenomenon, where a particle can pass through a potential barrier even though its energy is smaller than the potential energy of the barrier i.e. $E < V_0$. Let's consider a one dimensional situation where a particle is initially located at the negative x-axis and the potential is

$$V(x) = \begin{cases} V_0 & ,\text{if } 0 \leq x \leq d \\ 0 & ,\text{otherwise} \end{cases} \tag{7}$$

This situation is represented graphically in Fig. 2. Classically a particle could only escape to region $x > d$ if its energy were higher than the potential

energy of the barrier $E > V_0$. Otherwise it would be just reflected back from the wall. In quantum mechanics, however, there is a finite probability for the particle to pass through the region $0 \leq x \leq d$ and escape. Starting from the time-independent Schrödinger equation [21]

$$\left(-\frac{\hbar^2}{2m}\nabla^2 + V(x)\right)\psi(x) = E\psi(x) \tag{8}$$

we can solve for the wave function of the particle for each region. This gives

$$\psi(x) = \begin{cases} Ae^{ikx} + A'e^{-ikx} & , x < 0 \\ Be^{-\kappa x} + B'e^{\kappa x} & , 0 \leq x \leq d \\ Ce^{ikx} & , x > d \end{cases} \tag{9}$$

where $k = \sqrt{2mE}/\hbar$ and $\kappa = \sqrt{2m(V_0 - E)}/\hbar$. Constants A, A', B, B' and C can be determined from the condition that the wave function and its first derivative must be continuous at $x = 0$ and $x = d$. In this situation particle can either be reflected from the barrier or transmitted through it and the corresponding terms can be found from the wave function for each case. The term with the amplitude A is the incoming wave, A' is the reflected wave, and C corresponds to the transmitted wave. Reflection and transmission coefficients are defined as $R = \frac{|A'|^2}{|A|^2}$ and $T = \frac{|C|^2}{|A|^2}$ and they represent the probability for each event to happen. Intuitively they must fulfill the condition $R + T = 1$ i.e. a particle is either reflected or transmitted. After the coefficients are determined, the following equation is acquired for the transmission coefficient i.e. the tunneling probability

$$T = \frac{|C|^2}{|A|^2} = \frac{1}{1 + \frac{1}{4}\frac{V_0^2}{E(V_0 - E)}\sinh^2(\kappa d)}. \tag{10}$$

Additionally, if we approximate that $\kappa d >> 1$ as is typically the case, the tunneling probability becomes

$$T \approx \frac{16E(V_0 - E)}{V_0^2}e^{-2\kappa d}. \tag{11}$$

It is important to note that the tunneling probability decreases exponentially as a function of barrier thickness d.

2.3 Tunnel Junctions

Typically, tunnel junctions consist of two conductors separated by a thin insulating barrier [22] (Fig. 3). Current can flow from one conductor to the other via quantum mechanical tunneling. Either one of the conductors can be a normal metal or a superconductor, and each variation corresponds to a different type of tunnel junction. Simplest case is the normal metal-insulator-normal metal, i.e. NIN junction, where both metals are non-superconducting. In a NIS junction, one of the normal metals is replaced by a superconductor, and a SIS junction contains two superconducting electrodes. Next, tunneling is described briefly in the first two cases. NIS junctions are the ones used in cooling applications and also in this work. It is still useful to start with simple NIN junctions when developing the description for tunneling current, since it can be easily modified for NIS junctions as well. SIS junctions are not discussed here, since they are not important regarding the scope of the thesis.

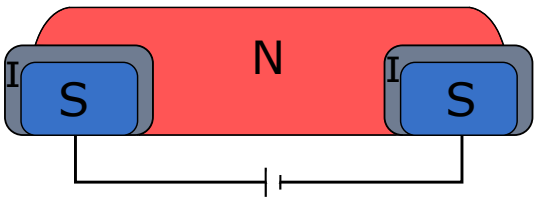

Figure 3: *General representation of a pair of NIS tunnel junctions. S is the superconductive electrode, I the insulating layer and N the normal metal. A voltage is applied across the junction to bias it.*

2.3.1 NIN Tunneling

Let's consider two normal metals separated by an insulator where an incident electron of energy E is located in metal 1 and is about to tunnel to metal 2. Tunneling is possible if there are empty states in metal 2 at the same

energy E. The rate of tunneling is proportional to number of occupied states in metal 1 at energy E and to number of empty states in metal 2 at energy E [19]. Occupation of energy levels is described by the Fermi function

$$f(E,T) = \frac{1}{e^{E/k_BT} + 1} \tag{12}$$

where k_B is the Boltzmann's constant. Energy E is measured relative to the Fermi energy i.e. $E(E_F) = 0$. In general, $E = \epsilon - \mu$, where ϵ is the energy and μ the chemical potential. The Fermi function gives the fraction of states of energy E that are occupied at temperature T. At 0 K all the states below the Fermi energy E_F are occupied and all the higher energy states empty. When applying a voltage i.e. biasing the junction, the local Fermi levels of the metals are shifted in energy relative to each other. The magnitude of the shift is eV, where e is the elementary charge and V the bias voltage. Figure 4 shows a schematic representation of a biased NIN junction at 0 K with occupied and unoccupied states visible.

In an ideal tunnel junction all the current comes from tunneling electrons from metal 1 to metal 2 and vice versa. At 0 K there is no tunneling when the junction is unbiased i.e. V = 0. At all temperatures tunneling increases with increasing bias voltage because there are more electrons in occupied states in metal 1 and more unoccupied states in metal 2 at the same energy.

At finite temperatures, the electrons have thermal energy, so some of them can move to states above the Fermi energy. The occupation of energy levels is then changed from the 0 K case and it is described by the Fermi function (eq. (12)). The tunneling rate from metal 1 to metal 2 is therefore [19], [14]

$$\Gamma_{12} = \Lambda|T|^2 N_1(E - eV) f_1(E - eV) N_2(E)(1 - f_2(E)) \tag{13}$$

where Λ is a proportionality constant and T a tunneling amplitude. The first part (functions with a subscript 1) is the number of occupied states in metal 1 and the second part (subscript 2) is the number of empty states in metal

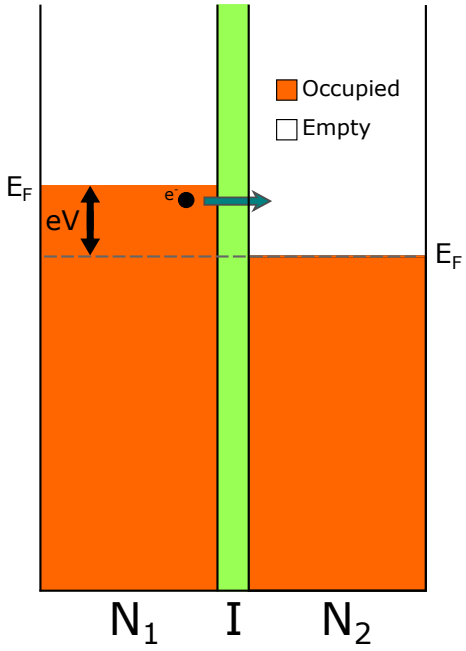

Figure 4: *A tunneling event in a NIN (normal metal-insulator-normal metal) junction at* 0 K. *The junction is biased with a voltage* V. *Occupied and empty states are also shown.*

2. The tunneling rate from metal 2 to metal 1 can be constructed similarly

$$\Gamma_{21} = \Lambda|T|^2 N_1(E - eV)(1 - f_1(E - eV))N_2(E)f_2(E). \tag{14}$$

The net current from metal 1 to metal 2 is the difference in tunneling rates i.e. $\Gamma_{12} - \Gamma_{21}$ integrated over all energies E so the total current through a NIN junction is

$$I = \Lambda|T|^2 \int_{-\infty}^{\infty} N_1(E - eV)N_2(E)[f_1(E - eV) - f_2(E)]dE. \tag{15}$$

By using the equation for the density of states and the Fermi function equation (15) can be integrated. The density of states of a normal metal varies only slowly with temperature for $T << T_F$ so we can thus replace $N_1(E-eV)$

and $N_2(E)$ with $N_1(0)$ and $N_2(0)$. The result is

$$I = \Lambda|T|^2 N_1(0)N_2(0)\int_{-\infty}^{\infty}[f_1(E-eV) - f_2(E)]dE \tag{16}$$

$$= \Lambda|T|^2 N_1(0)N_2(0)eV. \tag{17}$$

In other words NIN junction behaves like an ohmic resistor with $R = 1/\Lambda|T|^2 N_1(0)N_2(0)$.

2.3.2 NIS Tunneling

A NIS junction has one normal metal and one superconducting electrode. If the junction is unbiased (no voltage applied) the Fermi levels of the electrodes are located at the same energy. In the superconductor this is at the middle of the energy gap so there are no empty states available. In other words, there is no current at zero bias. When voltage is applied, the Fermi level of the normal metal can be raised and, electrons will tunnel from the normal metal to the superconductor. Because of the energy gap, tunneling is possible only if $eV > \Delta$. Figure 5 shows a schematic representation of a tunneling event in a NIS junction.

As was the case with NIN junctions, tunneling rate is proportional to the number of occupied states at the initial electrode and to the number of empty states at the final electrode, which in a NIS junction are the normal metal and the superconductor respectively. Occupied and empty states for both electrodes are also shown in Fig. 5. A description for the tunneling current can be deduced from equation (15) but now properties which include metal 2 are changed into properties of the superconductor (subscript S). Everything containing only metal 1 remains unchanged (subscript changed to N) but the density of states for the superconductor is strongly energy and temperature dependent so equation 6 is used to account for that. The current through a NIS junction then becomes [23]

$$I(V,T) = \frac{1}{eR_T}\int_{-\infty}^{\infty} n_S(E)[f_N(E-eV) - f_S(E)]dE, \tag{18}$$

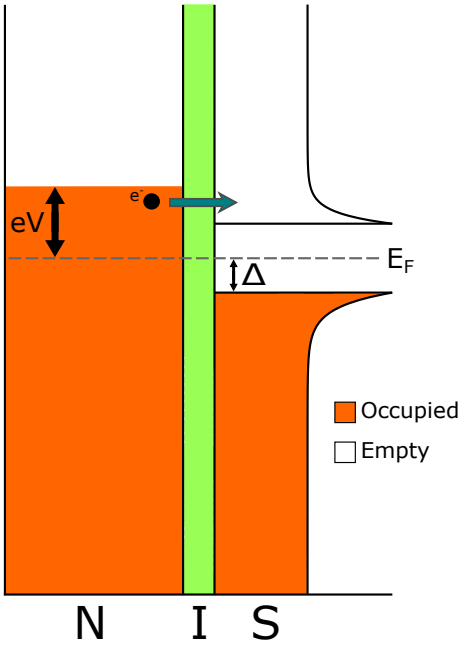

Figure 5: *Tunneling event on a normal metal-insulator-superconductor (NIS) junction. The junction is biased with a voltage V. Occupied and empty states are shown.*

where n_S is the normalized density of states of the superconductor, f_N and f_S are the Fermi functions for the normal metal and the superconductor respectively. R_T is the tunneling resistance which has the form [24]

$$R_T = \frac{\hbar}{4\pi e^2 A |T|^2 N_N(0) N_S(0)}. \tag{19}$$

Here A is the area of the tunnel junction and T the tunneling amplitude. As can be seen from equation (5) and Fig. 5, the largest number of energy states in the superconductor are located just above and below the energy gap i.e. $E \approx \pm\Delta$. That is why small changes in bias voltage near $V \approx \Delta/e$ produce large changes in tunneling current.

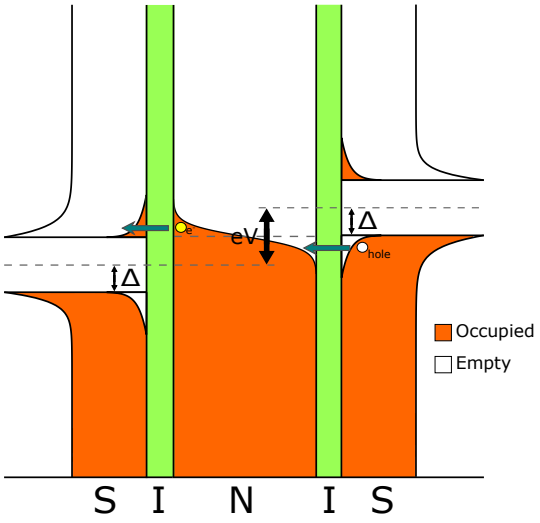

Figure 6: *Representation of two NIS junctions in series forming a SINIS structure.*

2.3.3 SINIS Coolers

NIS junctions can be used especially in thermometry or cooling applications. Cooling of the normal metal is achieved because of the energy gap of the superconductor. When an appropriate voltage bias is applied across the junction so that only the occupied states in the normal metal with the highest energy are above the energy gap of the superconductor, only the hot electrons in these states can tunnel through the potential barrier. These high energy electrons are now away from the normal metal, the average kinetic energy of the electrons is lowered which results to lower electronic temperature of the normal metal.

Usually, two NIS junctions are used in series forming a SINIS structure where the normal metal is located between the two superconductors. This makes it possible to achieve higher cooling powers because the voltage drop across a SINIS structure is twice of that of a single NIS junction. The operation principle of a SINIS structure is shown in Fig. 6. The reason why also SINIS junctions can be used as coolers is because the cooling power is symmetric in bias voltage [25]. Hot electrons tunnel from the normal metal to one superconductor and at the same time low energy holes below the en-

ergy gap tunnel from the other superconductor to the normal metal which also gives rise to cooling.

An expression for the cooling power can be achieved by modifying equation (18). We can multiply it by a term $\frac{eV-E}{e}$ where the numerator is the energy removed or added to the normal metal, and by dividing it with the electron charge e we get the energy in the units of voltage. That way the equation for cooling power can be thought as the voltage multiplied by the current which is the standard formula for electrical power. So the cooling power for a single NIS junction is [26]

$$\dot{Q}_{NIS}(V, T_{S,e}, T_{N,e}) = \frac{1}{e^2 R_T} \int_{-\infty}^{\infty} (E-eV) n_S(E) [f_S(E, T_{S,e}) - f_N(E-eV, T_{N,e})] dE. \tag{20}$$

The cooling power of an ideal SINIS structure is twice the cooling power of a single junction. Cooling power reaches its maximum when $T \approx 0.4 T_C$ and $V \leq \Delta/e$. Then equation (20) becomes [27]

$$\dot{Q}_{max} \approx 0.6 \frac{\Delta^2}{e^2 R_T} \left(\frac{k_B T_{N,e}}{\Delta} \right)^{3/2}. \tag{21}$$

From equation (21) it can be seen that the maximum cooling power is directly proportional to the square root of the energy gap and inversely proportional to the tunneling resistance i.e. $\dot{Q}_{max} \propto \frac{\Delta^{1/2}}{R_T}$. In other words, cooling power can be increased by increasing the energy gap (using materials with large gaps e.g. niobium) or decreasing the tunneling resistance, and according to equation 21 that can be done by increasing the junction area.

2.4 Electron Beam Lithography

Lithography is a widely used method in the industry and in academic research. It makes it possible to draw a pattern with a computer and copy it onto a sample chip which can then be processed further. Using this technology it is possible to fabricate micro- and nanometer-scale structures e.g. electrical circuits. Two of the main branches of lithography are photolithography and electron beam (e-beam) lithography. In both of these, a sample

is first coated with a material called resist which undergoes a reaction when exposed to either light (usually UV) or an electron beam. Typically this reaction involves either bond breaking (exposed resist becomes more soluble) or cross-linking (resist becomes more insoluble). Now, if only some areas on the sample are exposed, the resist can be removed selectively because of the different solubility.

Photolithography uses ultraviolet light for exposure. The method is mainly used in the industry for its efficiency of creating large amount of structures in a short time. In photolithography the whole sample is illuminated at the same time and a special mask is used to prevent light from reaching areas that are to be left unexposed. However, these masks are often done with electron beam lithography. Because of that, optical lithography is good for creating large amounts of the same predetermined structures when modifications to them are seldom needed. The main disadvantage of photolithography is the wavelength of light, which determines the smallest possible linewidth that can be reached.

A scanning electron microscope (SEM) is used in e-beam lithography to expose the resist. The sample is illuminated with a focused electron beam one point at a time moving the beam across the sample. This makes the exposure time higher than in photolithography, but modifications to the patterns are easy to make. Unlike photolithography which can be done in air, e-beam lithography needs a good enough vacuum because the electrons would scatter with air molecules and exposure would not be possible. E-beam lithography is not, however, limited by the wavelength of light, so linewidths even smaller than 10 nm can be reached [28]. The limitations come from the aperture size in the SEM, aberrations in the electron optics and electron scattering, for example. Electron beam lithography is mainly used in research.

2.4.1 Substrate Cutting and Resist Spinning

E-beam lithography can be divided into several steps which are shown in Fig 7. First one is substrate cutting, where suitably sized sample chips are cut from a larger wafer. Almost any material can be used as a substrate, as long

as it has a smooth enough surface. By far the most common material is silicon which is used especially in electronics. Si wafers are typically 100 - 300 mm in diameter, and they are often coated with either silicon oxide or silicon nitride to make them non-conductive. Wafers are cut with a specialized tool and then cleaned to remove any dust and other impurities from the surface.

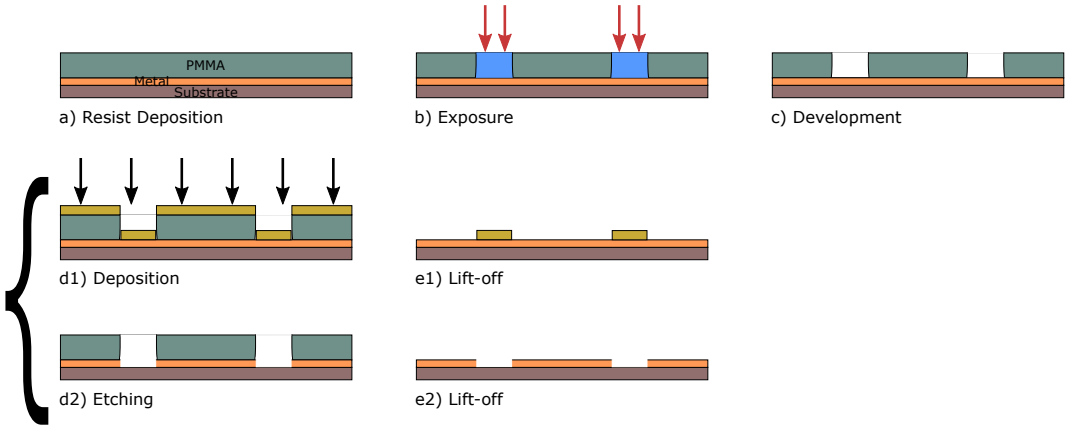

Figure 7: *Typical steps in an electron beam lithography process. a) Resist is deposited on a substrate (metal layer is there just for illustrative purposes). b) Resist is exposed with a SEM. c) Exposed resist is removed in development. d1) Depostion and etching are alternative process routes. Metal or another material is deposited on the substrate. e1) Remaining resist is removed in lift-off, also removing excess metal. d2) Material is etched away from regions not protected by the resist. e1) Excess resist is removed.*

After the substrates are cut and cleaned, a resit is deposited on top of them using a specific spin-coating apparatus. Several droplets of the resist are deposited on the chip which is placed on the stage of the spin-coating apparatus. After that the sample is rotated with specific angular velocity so that the resist spreads evenly on the surface. With angular velocity one can control the thickness of the formed resist layer. After the spin-coating, resist is often baked i.e. heated to a resist specific high temperature in order to remove the solvent and to harden the resist layer.

Resists are polymers diluted to a solvent forming typically a viscous solution [28]. There are many different types of resists for various purposes. These can be divided into two main categories: positive and negative resists.

Positive resists become soluble to its developer when exposed to an electron beam, which means that the resist is removed from the illuminated areas in the development step. Negative resist, however, becomes insoluble to its developer during exposure, so in that case resist is removed from unexposed areas of the sample. Using an appropriate mask or pattern, one can control which areas of the resist are exposed, making it possible to design complex structures that are then drawn on the sample. It is often useful to use two resists (or more) on top of each other, which enables the creation of even more complex structures and can make the lift-off step easier.

2.4.2 Exposure and Development

After spin-coating the resist can be exposed. This is done with a SEM. The electron beam selectively illuminates the areas determined by the designed pattern. Suitable magnification is selected depending on the width of the structures. There are also other factors that must be taken into account. For example, some resists are more sensitive to the electron beam than others. That is why there is an option in the software to change the resist sensitivity, which affects the time how long the beam spends in one location. Exposure time can also be controlled by dosage. It is possible to set different doses for different parts of the pattern if needed. Because the changes in resist polymers essentially happen because of the energy they receive from the electron beam, the beam current affects the exposure time as well. The larger the current, the less time the exposure will take. Current can be increased by increasing the spot size of the electron beam, but the width of the structures limits how large the spot size can be. It is important not to over-expose the resist, because that will affect the size and the sharpness of the pattern. Sometimes several layers of lithography are needed for the sample, and in that case it is crucially important to be able to align the new layer accurately in relation to the previous one. For that purpose, alignment marks are drawn on the first layer, and those are used to find the origin for the exposure pattern on the next layers.

After exposure, the sample undergoes a development step. It is deposited

in a developer solution of the resist for a sufficient amount of time. Developer dissolves either the exposed or unexposed resist depending on if the resist is positive or negative. There are typically two developers where the first one is usually unselective developing both layers of resist (if two layers are used) at same efficiency. Second developer, however, is highly selective and it only develops the resist underneath the first layer. This forms an undercut profile where the second layer is more developed than the first. This is used particularly for samples where metal is evaporated at an angle other than the normal angle. It also makes lift-off process easier.

2.4.3 Evaporation

At this point the sample has been patterned with the designed pattern, and it can be processed further. In other words, materials can either be deposited on the sample or removed from it, where the latter is called etching. Deposition can be done in many ways, but the relevant method for this work is evaporation.

In evaporation a solid metal (or another material) in a crucible is heated until it starts to evaporate. This is often done with an electron beam. Electron beam evaporation needs a good vacuum ($P < 10^{-4}$ mbar) so that the evaporated atoms do not collide with another atoms or molecules. Atoms travel from the crucible in a straight path to the sample which is located above the crucible a small distance away. Evaporation is a line-of-sight technique, which means that only the surfaces facing the crucible are coated with the evaporated material. There is a shutter between the crucible and the sample for controlling when the atoms can reach the sample.

Three different e-beam evaporator apparatuses are used in this work. UHV (ultra high vacuum) evaporator has a separate loading and evaporation chamber. The loading chamber is pumped with a rough pump and a turbo pump, and there is also a cryo pump for the evaporation chamber. Only the loading chamber is vented into atmosphere prior loading and unloading, while the evaporation chamber is always at high vacuum. That way pressures as low as 10^{-9} mbar can be reached. There is a gate valve between the

chambers for transferring the samples between them. The loading chamber is also connected to an oxygen line, which can be opened in order to oxidize the sample surface if needed.

The other two evaporators are Balzers (BAE 250) and Edwards (Edwards Auto 360). These can reach pressures of around 10^{-5} mbar. They have only one chamber which can be vented to atmosphere and pumped to the final pressure. Both are equipped with a rough pump and a turbo pump. In Balzers, the sample stage can be easily rotated and tilted if needed. Balzers is used especially for the evaporation of insulator materials. Edwards is also equipped with an oxygen line for oxidation, but that is not used in this work. All the evaporators use cold water for cooling the electron gun during evaporation.

2.4.4 Etching

In etching, material is removed either chemically or physically. Resist is protecting the sample so that only the areas where it was removed in development are exposed to the etchant. Etching can be divided into two categories: wet and plasma (dry) etching.

In wet etching the etchant is in liquid form. There are different etchants for different materials, and almost any material can be etched with a right recipe. There are many different factors affecting the etching rate and profile and some of them are not well understood. Most commonly, etching rate is increased by increasing temperature and/or etchant concentration. Most of the wet etching recipes have more or less isotropic profile, which means that the etching reaction progresses spherically in all directions. In practice this means that the sample is etched below the resist forming an undercut structure.

Plasma etching is done in a vacuum chamber with reactive gases, which is why it is often called reactive ion etching (RIE). RF electric field is used to detach electrons from gas atoms creating a plasma. This will also create excited gas molecules that are really reactive. Due to their small mass, electrons are fast enough to hit the chamber walls during the cycle of the

electric field. The chamber is connected to a ground potential whereas the sample stage is electrically isolated so electrons hitting it will create a negative potential. That will attract positively charged ions toward the sample and eventually they will hit it. The mass of the ions is so large that they do not have time to move very much due to the electric field alone. The ions will provide energy the the surface and also improve the directionality of the etching. That is why plasma etching is usually more anisotropic than wet etching. Etching in RIE is mostly due to the reactive gas molecules, and not so much due to the ions.

The last step in a lithographic process is called lift-off where all the remaining resist is removed. If something was deposited on the sample, this step removes all that material from places where there was resist underneath. After that the sample is ready for measurements or additional lithography layers.

2.5 Dilution Refrigerator

^{3}He-^{4}He dilution refrigerator is based on the mixing of the two helium isotopes ^{3}He and ^{4}He [29]. With such a device temperatures as low as ≈ 2 mK can be reached. There are methods such as nuclear demagnetization which can go even lower than that, but in many cases a temperature of a few millikelvins is low enough. Dilution refrigeration can be operated continuously, which is a great advantage against most of the other methods below 1 K. It is actually the only continuous cooling method for temperatures below 300 mK. That and its relatively simple design are some of the reasons why it is the most important refrigeration technology between temperatures 5 mK and 1 K.

Cooling power in a dilution refrigerator is provided by the enthalpy of mixing of the two helium isotopes. At temperatures below 870 mK, ^{3}He-^{4}He mixture separates into two distinct phases where one is ^{3}He rich, called the concentrated phase, and the another one is ^{4}He rich, called the dilute phase. ^{3}He is lighter of the isotopes so the concentrated phase is located above the dilute phase. When temperature is lowered even further ($T \to 0$),

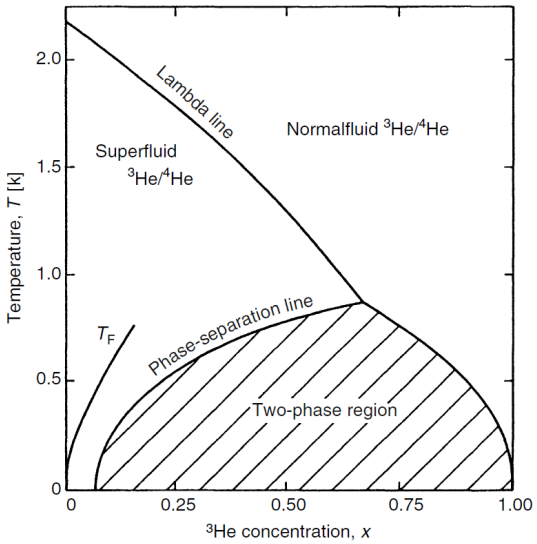

Figure 8: *Phase diagram of* ^{3}*He-*^{4}*H mixture. The mixture separates into two phases below* 0.87 K. *Figure obtained from [29].*

the concentrated phase becomes pure ^{3}He but there is still some ^{3}He left in the dilute phase. The phase diagram of ^{3}He-^{4}He mixture is shown in Fig. 8. If ^{3}He atoms are removed from the dilute phase, more will transfer from the concentrated phase to replace them in order to maintain the equilibrium. Cooling power comes from the enthalpy difference of the two phases and it is

$$Q = \dot{n}_3[H_d(T) - H_c(T)] \tag{22}$$

where $\dot{n}_3$ is the molar flow rate of ^{3}He, H_d and H_c are the enthalpies of the dilute and concentrated phases respectively. In the ideal case by using expressions for the enthalpies [29], the cooling power becomes

$$Q \approx 84\dot{n}_3 T^2. \tag{23}$$

The principal parts of a dilution refrigerator are shown in Fig. 9. The lowest section is the mixing chamber, which is also the coldest part of the refrigerator. The helium mixture is located there and this is the part that provides the cooling power. The mixing chamber is usually connected to

a sample stage with a material of high thermal conductivity to efficiently transfer heat out of the sample. Mixing chamber is also connected to the still via a capillary that is long enough to reach the dilute phase in the mixing chamber. Between the still and the mixing chamber there are several heat exchangers. The still is at relatively high temperature ≈ 0.7 K. At that temperature the vapor pressure of ^{3}He is much higher than that of ^{4}He. Still is connected to a pump located at room temperature. When the still is pumped, almost all of the vapor leaving the still is ^{3}He because of the large vapor pressure difference.

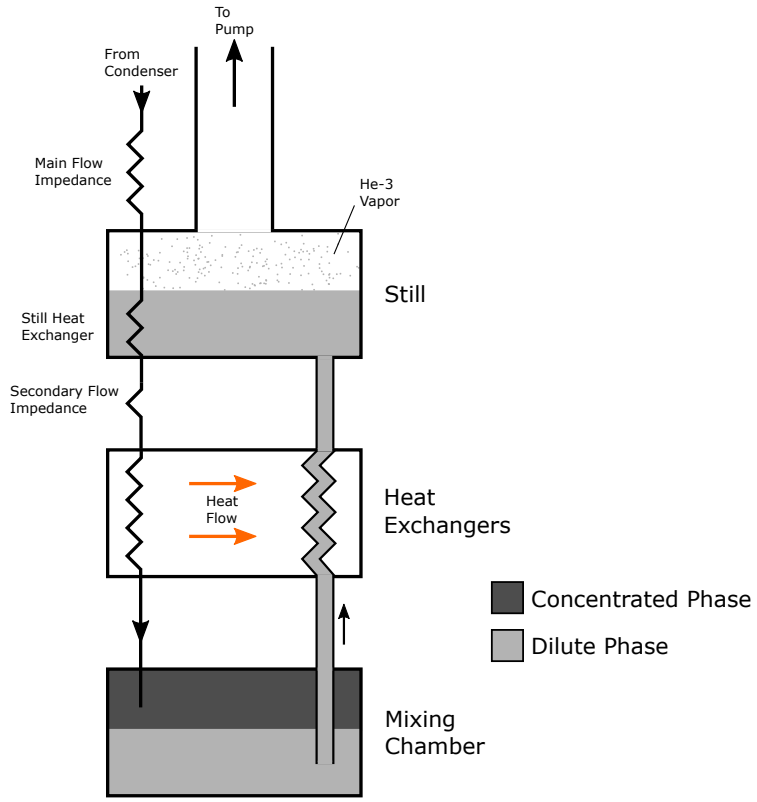

Figure 9: *Schematic representation of a ^{3}He-^{4}H dilution refrigerator. Concentrated and dilute phases are shown in different colors.*

When ^{3}He concentration in the still decreases, that creates an osmotic pressure difference between the still and the mixing chamber. That drives more ^{3}He atoms from the dilute phase of the mixing chamber to the still.

In order to keep the equilibrium, more ^{3}He must cross the phase boundary from the concentrated phase to replace the lost ^{3}He atoms. When ^{3}He vapor is pumped away from the still it will go through the room temperature parts after which it is directed into the cryostat again. First, it is precooled by a liquid ^{4}He bath to 4.2 K. Then the vapor is condensed in a continuously operating ^{4}He refrigerator (usually called the pot) working at ≈ 1.5 K. Immediately after the pot, there is a narrow capillary called the main flow impedance. That keeps the ^{3}He pressure high so that it will condense in the pot. Then ^{3}He (now in liquid form) goes through a heat exchanger connected to the still. Below the still there are several heat exchangers to cool the incoming liquid even further. The cooling is provided by the cold liquid that is leaving the mixing chamber. After the last heat exchanger ^{3}He enters the concentrated phase in the mixing chamber. That completes the operational cycle of a dilution refrigerator.

3 Experimental Methods

3.1 Sample Fabrication

In this work, SINIS tunnel junctions were fabricated with electron beam lithography. Both Al/AlO_x/Cu and Nb/Al/AlO_x/Cu junctions were fabricated with a method derived from ref. [7]. The former type of junction has aluminum as a superconducting electrode, while the latter has niobium. They are named in the following chapters as Al and Nb samples respectively. The fabrication procedure for both types of junctions is very similar. The largest difference is that for Nb junctions, a thin layer of aluminum is deposited on top of Nb layer, because a good quality tunneling barrier cannot be achieved by oxidizing Nb [30].

3.1.1 Al Samples

The first step is to cut 10 mm x 10 mm Si substrates from a larger wafer. They were cleaned in hot acetone by wiping them gently with a cotton wool

stick. Then the sample chips is put into isopropanol (IPA) and sonicated for 5 minutes (FinnSonic m03). Lastly they were dried with N_2 gas. The cleanliness of the samples was checked with an optical microscope. If they were not clean enough, CO_2 snow jet cleaning was used to clean them further. This last step was always able to remove most of the dirt from the sample.

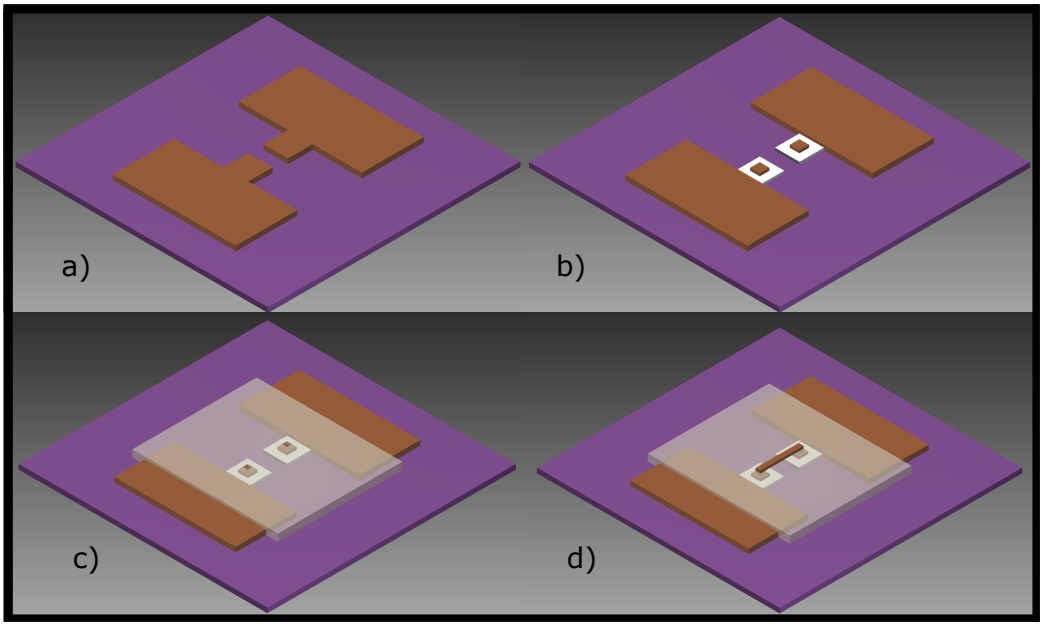

Figure 10: *All the different sample fabrication steps where every image corresponds to one complete set of lithography steps. a) Fabrication of contact pads and junction tri-layer. The silicon substrate is shown here in purple and brown is the junction tri-layer. b) Etching of the copper to separate the junction from the contact pads. Here, white is the aluminum and aluminum oxide of the tri-layer. c) Evaporation of a passivation layer between the two NIS junctions. The passivation layer is shown in transparent white color. d) Connecting the two NIS junctions to form a SINIS structure. The new copper is also shown in brown.*

Sample fabrication consists of four complete lithography steps. Figure 10 shows the different steps. In the first one (layer 1) the junction tri-layer and contact pads are deposited (Fig 10a). The second layer is used to etch the junction, i.e. to separate it from the contact pads (Fig. 10b). In layer 3, an insulating SiO_2 layer is evaporated between the two NIS junctions (Fig.

10c). Finally, a strip of copper is evaporated to connect the two junctions to form a SINIS structure (Fig. 10d).

Aluminum samples Al1 and Al2 differ from each other by their different junction areas. Al1 has 60 μm x 60 μm junctions and Al2 30 μm x 30 μm junctions. There are also slight differences in their fabrication steps which are described later below.

Resist was deposited on the substrates using a spin-coating apparatus (Bidtec SP-100). For Al1 samples, a polymethyl methacrylate (PMMA) A7 resist in anisole was used. After spin-coating, the samples were baked on a hot plate at 115 °C. Table 1 shows the spinning speeds, baking times and the final resist thicknesses used for Al1 samples. Samples were exposed with a SEM (LEO 1430). A writefield of 1024 μm x 1024 μm was used for a single sample structure. Six structures were drawn on every sample chip. A magnification of 190 was chosen, since it has been proven suitable for that specific writefield. The acceleration voltage for electrons was 30 kV and beam spot-size 780. Typically a current of 8 -15 nA was used for exposure. Samples were developed in PMMA developer, consisting of methyl-isobutylketone and isopropanol in 1:2 ratio. Typical development time was between 45-60 s, after which the sample was immediately immersed in isopropanol to remove the developer. Then the samples were dried with N_2 gas. Every layer of lithography begins with resist spinning and then goes through the same exposure and development steps. Naturally a different exposure pattern was used in every layer. In addition, reactive ion etching (RIE) (Oxford Instruments: Plasmalab 80 Plus) cleaning was performed before every evaporation step to clean the exposed surfaces. O_2 was used in this cleaning process and the parameters are time: 30 s, power: 60 W and pressure: 40 mT. This is a premade recipe called O_2 clean PMMA in our RIE.

In the first layer, the junction tri-layer was evaporated using the UHV evaporator. The pressure during evaporation was usually $\approx 10^{-8}$ mbar. First, aluminum was evaporated from a 0 ° angle (perpendicular to surface), after which the sample was transferred back to the loading chamber and oxidized to form a thin layer of AlO_x on top. Then copper was evaporated again from a 0 ° angle on top of the oxide. Evaporation and oxidation parameters

Table 1: Resist spinning parameters for Al1 samples.

	Spinning Speed [rpm]	Baking Time [min]	Thickness [nm]
Layer 1	4000	4	400
Layer 2	4000	4	400
Layer 3	2000	5	600
Layer 4	2000	5	600

for all the layers are shown in table 2. Lift-off was performed by immersing the sample in hot acetone until all the excess metal is removed. That can be helped by using a syringe to spray acetone towards the sample. After that it was dipped into isopropanol and dried with N_2 gas.

Table 2: Evaporation parameters for Al1 samples.

	Thickness [nm]	Evap. speed [nm/s]	Power [kW]	P [mbar]
Al	90	0.4	0.51	$1.7 \cdot 10^{-8}$
AlO_X		Oxidation 20 min @400 mbar		
Cu	75	0.4	0.60	$1.8 \cdot 10^{-8}$
SiO_2	200	0.2	0.15	$1.7 \cdot 10^{-5}$
Cu	250	0.15	0.29	$2 \cdot 10^{-5}$

In layer 2, the sample was immersed into copper etchant (HOAc + 30% H_2O_2). Typical etching time was between 60 - 75 s, after which the sample was put into isopropanol and dried with N_2 gas. Completeness of the etching process was checked with an optical microscope, and the etching step was repeated if there was still copper left around the junction (Fig. 10b). This etchant should not attack the aluminum oxide layer under the copper. After etching was sufficient, the resist was removed by lift-off.

In layer 3, an insulation layer was evaporated between the two NIS junctions in every structure (Fig. 10c). The thickness of the layer must be higher than the thickness of the junction. SiO_2 was selected as an insulator. Evaporation was done with the Balzers evaporator (Bal-Tec BAE 250), and the stage was rotated the whole time to prevent SiO_2 from forming pinholes. The pressure in Balzers during evaporation was $\approx 10^{-5}$ mbar. Excess evaporated material and resist was removed by lift-off at the end of this lithography

layer.

In the last layer, electrical contact is made between the two NIS junctions by evaporating a copper strip between them. The contact area was cleaned in RIE before the evaporation as described before. This can help to make the copper-copper contact as good as possible. The thickness of the copper layer must exceed that of the previous SiO_2 layer. For Al1 samples this evaporation is also made with the Balzers evaporator. After lift-off the samples are ready for measurements.

Al2 samples were fabricated essentially the same way as Al1 samples, but with certain notable differences. For Al2 samples, a 4% homemade PMMA resist in chlorobenzene was used for all lithography layers. Baking was done at 115 °C. Parameters for resist spinning are shown in Table 3. The thicknesses of metal and insulator layers vary also, and those are shown in Table 4. Evaporation of copper in the last layer was done with the Edwards evaporator (Edwards Auto 306) rather than Balzers, because the former provided more stable operation.

Table 3: Resist spinning parameters for Al2 samples.

	Spinning Speed [rpm]	Baking Time [min]	Thickness [nm]	Layers
Layer 1	3000	4	450	1
Layer 2	3000	4	450	1
Layer 3	1500	5	600	1
Layer 4	2500	5	500	2

Table 4: Evaporation parameters for Al2 samples.

	Thickness [nm]	Evap. speed [nm/s]	Power [kW]	P [mbar]
Al	50	0.15	0.93	$2.5 \cdot 10^{-8}$
AlO_X		Oxidation 20 min @400 mbar		
Cu	42	0.17	0.72	$3.0 \cdot 10^{-8}$
SiO_2	100	0.15	0.14	$1.5 \cdot 10^{-5}$
Cu	160	0.18	0.25	$2.3 \cdot 10^{-5}$

3.1.2 Nb Samples

Nb samples were fabricated the same way as the Al samples, the only difference being that Nb was evaporated as the superconducting electrode. A thin 10 nm layer of Al was also evaporated on top of the Nb, which is then oxidized to form the tunneling barrier. Since the thickness of the junction is different, the resist thicknesses were also changed from the values used for Al samples. The parameters for resist spinning are shown in Table 5. Table 6 shows the evaporation data for all the lithography layers.

Table 5: Resist spinning parameters for Nb samples.

	Spinning Speed [rpm]	Baking Time [min]	Thickness [nm]
Layer 1	3000	4	450
Layer 2	4000	4	400
Layer 3	2500	5	500
Layer 4	2500	5	500

Table 6: Evaporation parameters for Nb samples.

	Thickness [nm]	Evap. speed [nm/s]	Power [kW]	P [mbar]
Nb	30	0.45	2.64	$4.3 \cdot 10^{-8}$
Al	10	0.1	0.55	$1.0 \cdot 10^{-7}$
AlO_X		Oxidation 20 min @400 mbar		
Cu	50	0.3	0.66	$8.0 \cdot 10^{-8}$
SiO_2	100	0.15	0.12	$2.8 \cdot 10^{-5}$
Cu	150	0.15	0.19	$1.8 \cdot 10^{-5}$

3.1.3 Problems During Fabrication

The yield of the fabrication process for both Al and Nb samples is strongly dependent on the human factor, and no two samples are exactly the same. Sometimes all of the samples in a batch were successful, and sometimes none of them, without any easily identifiable reason. One problem during fabrication was the temperature used in resist baking. Typically PMMA is baked at 160 °C but for these samples this was too high. After layer 1,

there was copper on the sample, and when that is exposed to a resist at high temperature, it did cause the copper to degrade. Lowering the temperature to 115 °C seemed to solve the problem.

3.2 Measurements

As soon as the fabrication was complete, all the sample structures were tested by measuring their electrical resistance at room temperature. This was done by using a multimeter (Fluke 75-III) which is attached to small probes that can be accurately moved to contact with the sample without damaging it.

Samples were cooled down with a dilution refrigerator PDR50. Before the cooldown procedure, there are preparations to be made. This cryostat has a sample stage with twelve lines that can be used for measurements. First, the samples to be measured are glued to the sample stage with a low-T glue (GE Varnish). Then the samples are electrically connected to the contact pads of the lines in the sample stage. Aluminum wire is used because it is superconducting at the measurement temperatures. The wires are connected with an ultrasound bonder machine (Kulicke & Soffa 4523A Digital) into a four-probe measurement configuration, i.e. there are two wires for current (I+ and I-) and two for voltage (V+ and V-). This way it is possible to conduct an accurate voltage measurement without the influence of the wire resistances. The sample stage was then connected to the cryostat, and the condition of the samples was tested, as well as the condition of different heaters and the RuO thermometer. The cryostat is precooled with liquid nitrogen to 77 K, and then with liquid ^{4}He to 4.2 K. The operation principle of a dilution refrigerator is explained in chapter 2.5.

3.2.1 $I(V)$ Measurements

Measurements were done in a shielded room. The measurement configuration is shown in Fig. 11. The voltage source is homemade, and it gives a triangular sweeping DC voltage. There is an input for superimposing an AC signal in the voltage source, but that is not used in the $I(V)$ measurements. Different voltage dividers were used to change the range of the voltage sweep.

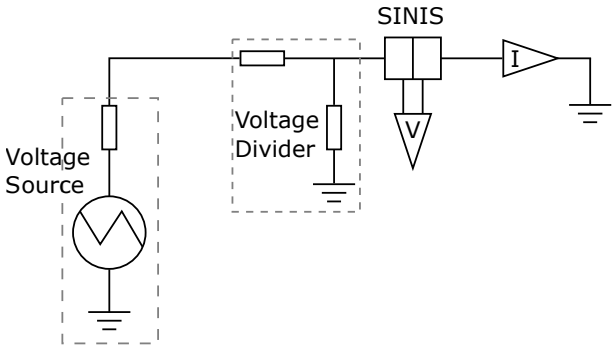

Figure 11: *Electrical circuit used in IV measurements. Different resistors were used in voltage division. Typically the division was between* 1/11 *and* 1/200*.*

Typically, the first resistor from the left in the divider was between 100 Ω - 2 kΩ and the second was 10 Ω. The voltage drop across the sample was measured with Ithaco 1201 Low Noise Preamplifier (High Pass: DC, Low Pass: 10 Hz, Type: DC), and the current with Ithaco 1211 Current Preamplifier (Suppression: off, Rise Time: 300 ms). The gain of the voltage amplifier was between $1 \cdot 10^3$ - $10 \cdot 10^3$, and the sensitivity of the current amplifier between $1 \cdot 10^{-3}$ - $10 \cdot 10^{-5}$ both depending on the voltage division. The resistance of the RuO thermometer was measured with AVS-47 Resistance Bridge. The measured resistance can be converted to temperature using a known calibration curve. All the outputs are connected to a multichannel ADC unit (National instruments) which transfers the data to computer's Labview program.

3.2.2 $dI/dV(V)$ Measurements

The $dI/dV(V)$ measurement configuration is shown in Fig. 12. An AC signal was generated with a lock-in amplifier (Stanford Research Systems SR810), and it is connected to the AC input of the homemade voltage source. That ads the AC signal on top of the DC sweep. Different voltage dividers were used after the lock-in amplifier output and the voltage source to get desired AC and DC signals. Typical DC dividers are presented in section 3.2.1, and either a 250 Ω or a 1 kΩ resistor was used together with a 10 Ω resistor on

the AC side. The resistor R_0 before the sample represents the resistance caused by the cables and wiring, and it was 133 Ω. The DC voltage across the sample was measured as in the $I(V)$ measurement, but in addition, the AC voltage was measured with another Ithaco 1201 Low Noise Preamplifier (High Pass: 0.3 Hz, Low Pass: 300 Hz, Type: AC). The output of this was connected to input A of the lock-in amplifier. The settings used for the lock-in amplifier were: $V_{ex} = 1$ V or 1.8 V (at the lock-in amp), frequency: 20 Hz, time constant: 300 ms, and sensitivity: 50 μV - 500 μV. The excitation voltage at the sample was typically ≈ 300 μV. The output of the lock-in amplifier as well as sample DC voltage and RuO resistance are connected to the multichannel plate and read from a computer. This setup measures the differential resistance dV/dI but it is converted to conductance dI/dV in the results.

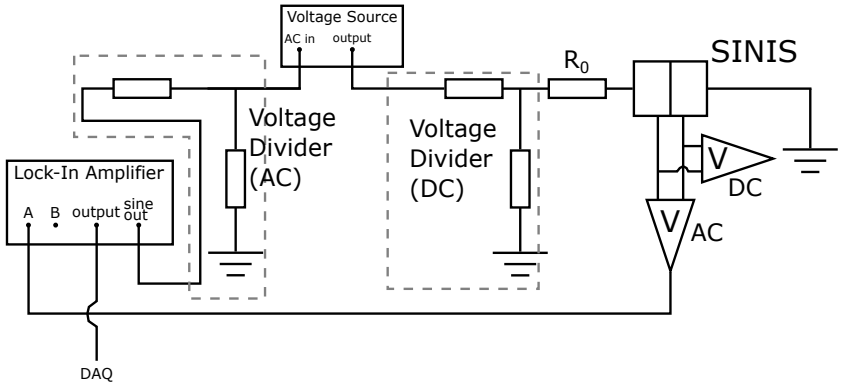

Figure 12: *Configuration used in the conductance measurements. Different resistors were used in the voltage divisions (AC and DC).*

4 Results

The measurements were conducted for two 60 μm x 60 μm and for two 30 μm x 30 μm Al/AlO_x/Cu junctions. The larger junctions are named Al1A and Al1B, while the smaller are Al2A and Al2B. Also, two 60 μm x 60 μm Nb/Al/AlO_x/Cu junctions were studied. These are named Nb1A and Nb2B.

The current-voltage characteristics were measured for all the samples and the resulting IV curves are shown below. Also the derivative of the current i.e. differential conductance was calculated to determine the energy gap and the tunneling resistance. Differential conductance was also measured directly and compared to the calculated curves. At least one sample was then selected from each category (Al1, Al2 and Nb), and a theoretical fit was done using a model including thermal effects. Parameters from the model were used to construct a theoretical curve of the cooling power of these tunnel junctions.

4.1 Al1 Samples

4.1.1 $I(V)$ Measurements

I(V) measurements were done as described in section 3.2.1. The I-V curves for samples Al1A and Al1B are shown in Figure 13. Fig. 13a shows the IV on linear scale, while Fig. 13b gives the current in logarithmic scale. This data is used to calculate the derivative of current versus voltage (dI/dV) which is shown in Fig. 13c. The base temperature did not stay constant during the measurement, and the cryostat started to heat with increasing bias voltage. The temperature was between 98 mK - 270 mK for sample Al1A and between 104 mK - 177 mK for Al1B.

It can be seen particularly well from Figs. 13a and 13c that there is a relatively large current through the sample with voltages below the energy gap 2Δ which is typically 0.44 meV for aluminum. This current cannot be entirely caused by the presence of states in the energy gap which is taken into account by the Dynes parameter. This result suggests that there is a parallel resistance R_P in the sample. This means that current can flow through some other route, in addition to the predicted tunneling route between N and S electrodes with resistance R_T. This model is illustrated in Figure 14. The magnitude of R_P can be estimated from conductance data (Fig. 13c), because without parallel resistance, conductance should be close to zero in the middle region of the energy gap. For Al1A sample $R_P = 1.8\,\Omega$ and for Al1B $R_P = 2.2\,\Omega$. This constant resistance, which is inverse of conductance, can then be subtracted from the measured IV data. The corrected data

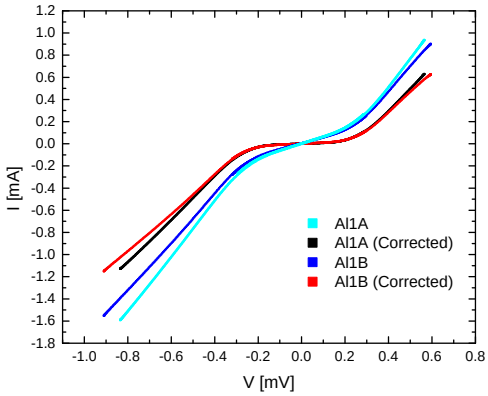

(a) IV on linear scale

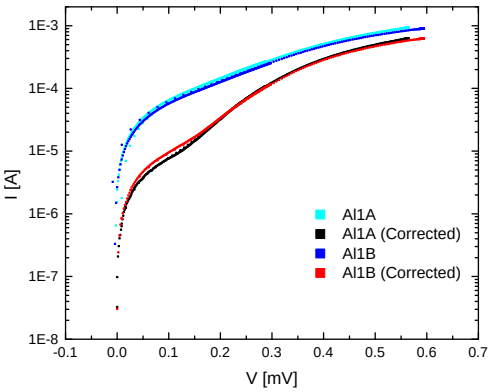

(b) IV on logarithmic scale

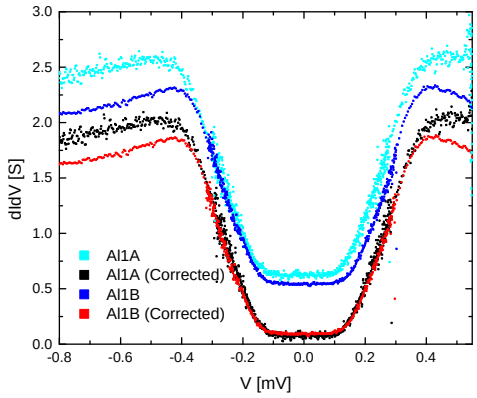

(c) Conductance calculated numerically from the IV

Figure 13: *Measured IV for Al1 samples. Also shows the data after the removal of parallel resistance (corrected data).*

for both samples is shown in Figures 13a - 13c. Conductance is corrected by removing a baseline of $1/R_P$ from the data, and similarly, a voltage dependent expression $\frac{1}{R_P}V$ is removed from the current to correct the IV.

Tunneling resistance R_T of the junction can be determined by making a fit to the linear part of the IV curve. This way we get $R_T = 0.6\ \Omega$ for Al1A and $R_T = 0.7\ \Omega$ for Al1B. Value for the energy gap Δ is obtained from conductance data. It is centered symmetrically around zero bias voltage and

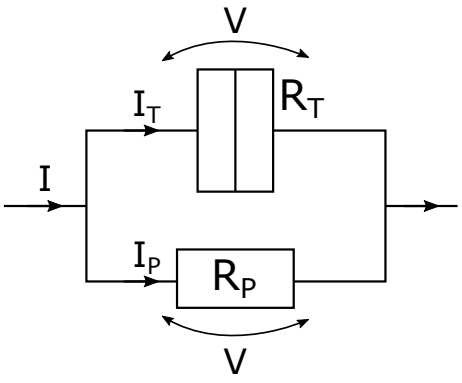

Figure 14: *Model for parallel resistance R_P.*

for a SINIS junction the observed gap is 2Δ due to the presence of two NIS junctions. Because of the large temperature change due to self-heating, the gap feature is quite smeared. Here, it is defined from $V = 0$ as the point where conductance reaches its maximum value. This way, we get 0.4420 meV for Al1A and 0.4284 meV for Al1B which correspond to single junction values $\Delta = 0.22$ meV and $\Delta = 0.21$ meV respectively.

The current-voltage characteristics of Al1A and Al1B are very similar. Both samples clearly exhibit behavior associated with tunnel junctions, namely they have an energy gap Δ. Values of Δ for both samples are very close to the expected value 0.22 meV for aluminum. At $V > \Delta/e$ the current starts to increase rapidly, as more states become available for electron tunneling in the superconductor. Figure 15 shows the ideal SINIS behavior at different temperatures, calculated from equation (18). In ideal junctions, there should be a large peak in the conductance just after the energy gap. This feature is not fully present in these samples, since the conductance is almost flat after the gap. The shape of the IV and conductance at high bias voltages would suggest that the temperature of the junction is much higher than the base temperature of the cryostat. The low bias region of the IV is at much lower temperature, resembling SINIS behavior at the lowest base temperature ($\approx$ 100 mK for both samples) during the measurement. This can be seen especially from the logarithmic and conductance plots.

Tunneling resistances of Al1A and Al1B (0.6 Ω and 0.7 Ω respectively)

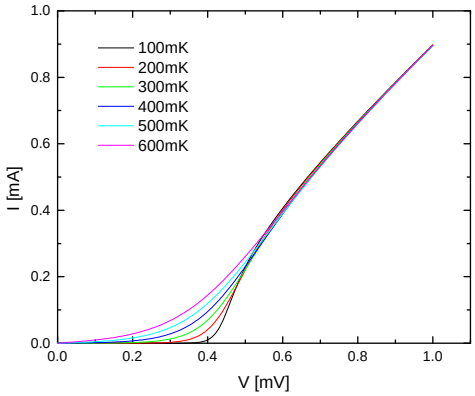

(a) IV on linear scale at different temperatures

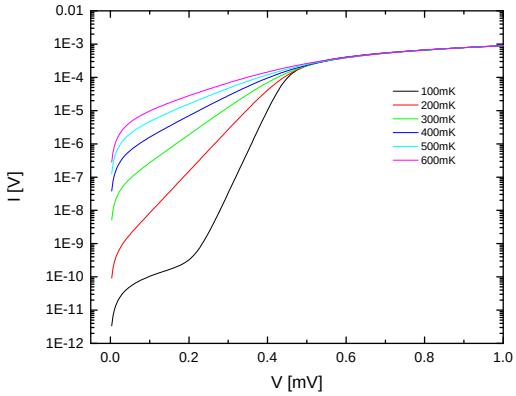

(b) IV on logarithmic scale at different temperatures

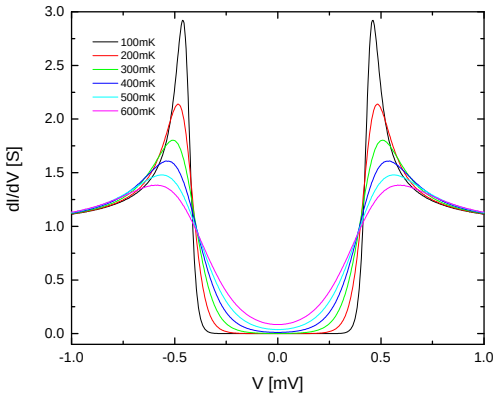

(c) Conductance at different temperatures

Figure 15: *Simulated plots of ideal SINIS behavior using typical values for large aluminum junctions. Here,* $\Delta = 0.22$ meV, $\Gamma = 1 \cdot 10^{-6}$ *and* $R_T = 1\ \Omega$.

are also very close to each other. These are also comparable to the parallel resistances of the junctions (1.8 Ω and 2.2 Ω). For Al1A, R_T is 33% of R_P and for Al1B the value is 29%. With small bias voltages i.e. in the gap, R_P is dominant over R_T, so a significant fraction of the current is flowing through the route associated with R_P. Since heating power is $P = IV$ this is a likely cause for the heating of the samples during measurement.

4.1.2 $dI/dV(V)$ Measurements

Conductance measurements were done with a lock-in amplifier as described in chapter 3.2.2. Only sample Al1A was measured. Figure 16 shows the obtained conductance plot which is given in real units. This data also confirms the encountered parallel resistance and the value is $R_P = 2.1\,\Omega$. This is relatively close to the value obtained from the IV measurement. The tunneling resistance for this sample is $R_T = 0.6\,\Omega$ and it is very similar to the IV value. The energy gap is determined the same way as before and this gives $2\Delta = 0.43$ meV which corresponds to a single gap value $\Delta = 0.22$ meV. This value is also in good agreement with IV measurement and the known value for Al energy gap. There is an additional feature at positive bias voltages $V > 0.4$ mV, where the current starts to rise rapidly at the end of the voltage sweep. This behavior is not observed at negative bias, as can be seen from Fig. 16. This behavior is not yet understood.

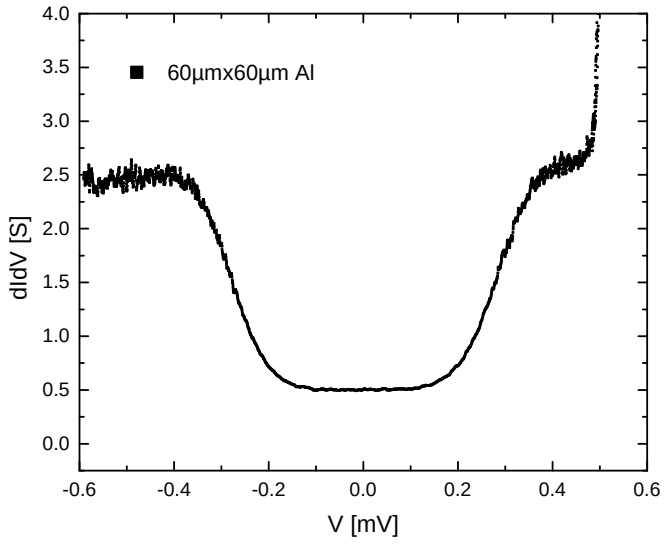

Figure 16: *Measured conductance of Al1A.*

4.1.3 Thermal Model Fit

Due to the large sample heating during the measurements, a standard BCS theory with constant temperature for SINIS junctions cannot be used for fitting. That is because the simple theory does not take into account any heating effects, and the only non-ideality it accounts for is the Dynes parameter, which is not enough for this situation. For that reason, a thermal model fit is used. The thermal model includes a power law and takes into account the finite size of the normal metal [19]. The power law is of the form [23]

$$P_{cool} = P_{heat}, \tag{24}$$

where P_{cool} is the cooling power of the junction (Eq. (20)) and P_{heat} is the heat flow from the surroundings. The latter can be expressed as

$$P_{heat} = -A(T_e^n - T_{bath}^n) + \beta(P_{cool} + IV), \tag{25}$$

where the first term represents the coupling between the electrons in the normal metal (at temperature T_e) and the environment (at temperature T_{bath}). A is the coupling strength, which is in most cases described by the electron-phonon coupling

$$A = \Sigma\Omega, \tag{26}$$

where Σ is the coupling constant and Ω the volume of the normal metal. n is between 4-6 depending on the scattering mechanism [31]. When electrons tunnel from normal metal to superconductor, some of these electrons may return back to the normal metal which causes heating. This is included in the thermal model by the second term in equation (25). The fraction of the power returned to the normal metal from the total amount deposited into the superconductor is represented with parameter β, where $0 \leq \beta \leq 1$, but it is typically quite small (≈ 0.05 for 100 μm^2 junctions [19]). IV represents the heating power (Joule heating) caused by the tunneling processes.

The thermal model fit was used for both Al1A and Al1B samples. The values used in the model were $n = 5$, $\Sigma = 1.8 \cdot 10^9$ (for Cu) and $V = 270$ μm^3. The IV plots with the thermal fit for Al1A is shown in Figure 17. Figs. 17a

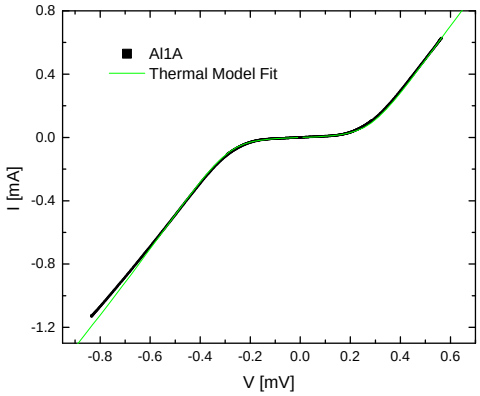

(a) IV on linear scale

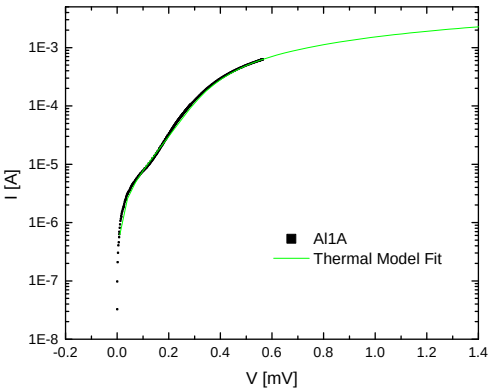

(b) IV on logarithmic scale

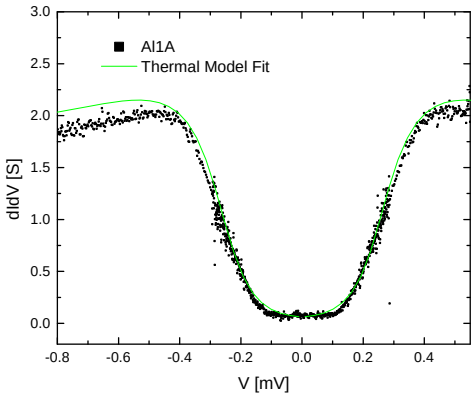

(c) Conductance calculated numerically from the IV

Figure 17: *Al1A IV data and the thermal model fit with parameters* $R_T = 0.6\ \Omega$, $\Delta = 0.22$ meV, $T_{bath} = 0.15$ K, $\Gamma = 4 \cdot 10^{-2}$ *and* $\beta = 0.7$.

and 17b show the IV behavior where the latter plot is logarithmic. Figure 17c shows the calculated conductance plot. Parameters for the fit are $R_T = 0.6\ \Omega$, $\Delta = 0.22$ meV, $T_{bath} = 0.15$ K, $\Gamma = 4 \cdot 10^{-2}$ and $\beta = 0.7$. Here T_{bath} is the starting temperature for the fit and it is typically very close to the bath temperature of the cryostat. Γ is the Dynes parameter and it is given in units relative to the energy gap i.e. Γ/Δ. The fit is in quite good agreement with the IV data even though there is some deviation as can be seen from

the logarithmic plot (Fig. 17b). The conductance data deviate much more from the fit especially at voltages above the energy gap. Also the measured energy gap is wider at the bottom of the gap than the corresponding fit. This indicates that the temperature is in reality somewhat lower than the fit indicates. Still, the fit is in good agreement along the walls of the energy gap ($0.2\ \mathrm{mV} \leq |V| \leq 0.4\ \mathrm{mV}$).

The value for β is 0.7 and this is really high indicating that 70% of the power deposited into the superconductor is returned back to the normal metal. It must be noted, however, that this model does not consider parallel resistances. It is used here to take into account the heating of the samples even though the mechanism for the heating process is not identical to that of the thermal model. In absence of the parallel resistance, β would most likely be significantly smaller.

Also the value for Dynes parameter is high for this sample. It might be due to the large junction area, but there is also the difficulty of determining how much of the subgap current is due to the parallel resistance, and how much is accounted by the Dynes parameter. By changing the value for R_P it is possible to get different values for the Dynes parameter. Still, the order of magnitude of Γ must be correct because with e.g. much lower values the features in the IV data would be much more distinguishable, and vice versa.

The data with the thermal fit for Al1B sample is shown in Figure 18. Linear and logarithmic IV plots are in Figures 18a and 18b respectively. Figure 18c shows the calculated conductance plot. Parameters for the fit are $R_T = 0.65\ \Omega$, $\Delta = 0.22\ \mathrm{meV}$, $T_{bath} = 0.11\ \mathrm{K}$, $\Gamma = 5 \cdot 10^{-2}$ and $\beta = 0.8$. These parameters are very similar to the ones used for fitting Al1A sample. Bath temperature is 40 mK lower but the Dynes parameter is changed from $4 \cdot 10^{-2}$ to $5 \cdot 10^{-2}$ and β from 0.7 to 0.8. These are, however, minor differences and cannot be attributed to any specific feature in the sample because of the ambiguity of choosing the value for the Dynes parameter, which was discussed earlier. The fit corresponds to the data in a very similar way as for Al1A sample. Namely, the fit follows the IV data quite well especially at small voltages and deviates more at high bias. Also the energy gap is better defined in the measured data than in the fit, even though the fit is good along

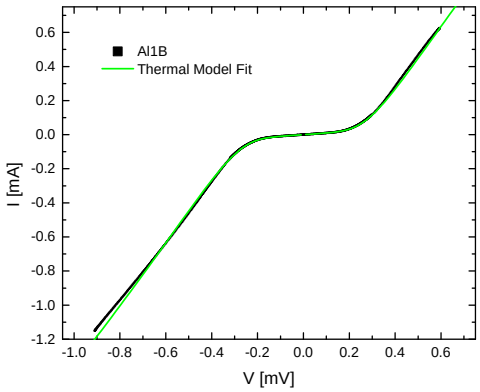

(a) IV on linear scale

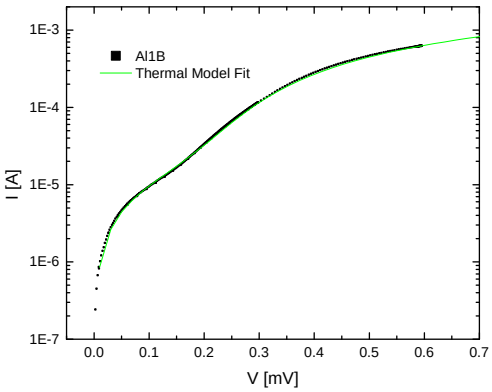

(b) IV on logarithmic scale

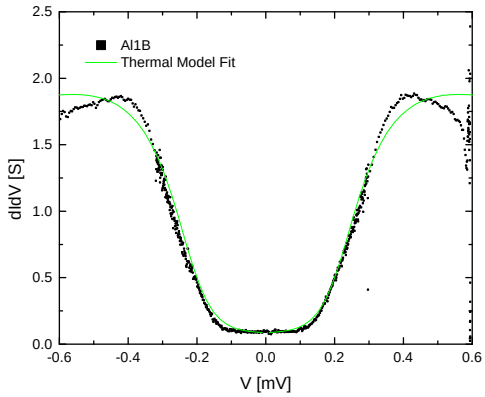

(c) Conductance calculated numerically from the IV

Figure 18: *Al1B IV data and the thermal model fit with parameters* $R_T = 0.65\ \Omega$, $\Delta = 0.22$ meV, $T_{bath} = 0.11$ K, $\Gamma = 5 \cdot 10^{-2}$ *and* $\beta = 0.8$.

the walls of the gap.

4.1.4 Cooling Power

Because of the parallel resistance and the large heating effect it causes, cooling cannot be observed for these samples. Still, the cooling power of similar devices without the parallel resistance can be estimated. Figure 19 shows the cooling power $-P_N$ of the normal metal as a function of bias voltage in a 60 μm x 60 μm Al/AlO_x/Cu SINIS junction that has a tunneling resistance of 0.6 Ω. The cooling power is shown in three different temperatures that are $0.2T_C$, $0.4T_C$ and $0.5T_C$ where T_C is the critical temperature of the superconductor. For aluminum these temperatures are 280 mK, 560 mK and 700 mK, respectively. Cooling powers are calculated with two different Dynes parameters: $3 \cdot 10^{-2}$ and $5 \cdot 10^{-2}$ which are typical for this type of junctions as seen from the measurement data. Otherwise ideal conditions are assumed, so e.g. the temperature of the superconductor and the normal metal are the same ($T_S = T_N$).

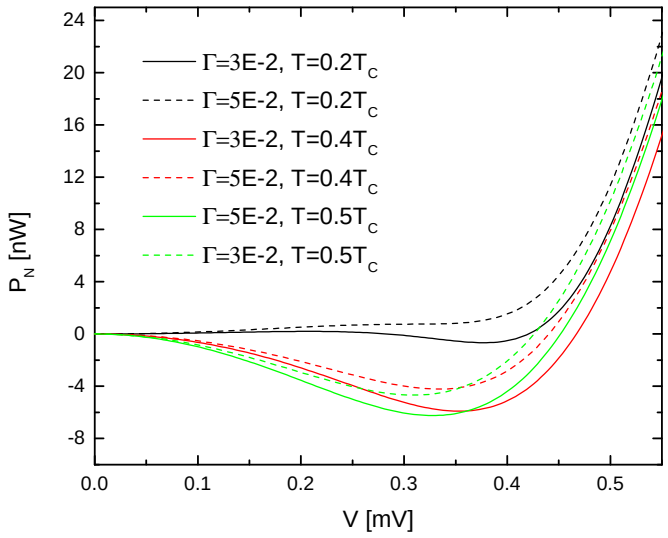

Figure 19: Calculated cooling power $-P_N$ of the normal metal for 60 μm x 60 μm Al SINIS tunnel junction at different temperatures. Typical values for the Dynes parameter are used.

Normal metal is cooled when P_N is negative i.e. power is removed from it. It can be seen from Fig. 19 that there is cooling in all cases expect when $\Gamma = 5 \cdot 10^{-2}$ and $T = 0.2T_C$ The cooling power becomes negative almost at zero bias in temperatures other than $0.2T_C$ where it starts at 0.28 mV. Largest voltage range for cooling is achieved at the temperature $0.4T_C$ while the maximum value for cooling power is reached at $0.5T_C$. The maxima in all cases occur at bias voltages small distance below the gap as predicted by the theory. At that voltage only the hot electrons are tunneling from the normal metal so the cooling effect is maximized. Cooling power is higher with smaller values of the Dynes parameters. The maxima at $0.4T_C$ are 5.9 nW and 4.2 nW, and at $0.5T_C$ 6.2 nW and 4.7 nW where the first value corresponds to the smaller Dynes parameter. The differences in these maxima are 1.7 nW and 1.6 nW respectively. This dependence in Dynes parameter is due to the fact that with higher values, more states are created within the energy gap allowing also cold electrons to tunnel to the superconductor, thus decreasing the overall cooling effect.

4.2 Al2 Samples

4.2.1 $I(V)$ Measurements

Current-voltage characteristics of Al2A and Al2B were measured the same way as for Al1 samples. The resulting IV plots are shown in Figures 20a and 20b in linear and logarithmic scales, respectively. Conductance (dI/dV) plots are calculated from the IVs and they are shown in Fig. 20c. The base temperature of the cryostat during AL2A measurement was 58 mK - 408 mK and for Al2B 58 mK - 403 mK.

Parallel resistance is present also in these smaller samples as can be seen from Fig. 20. It is removed in the same way as described in chapter 4.1.1. The corrected plots are also shown in Fig. 20. The tunneling resistances R_T measured from the IV characteristics are 9.2 Ω and 37 Ω for Al2A and Al2B respectively. The removed parallel resistances are $R_P = 10.5\ \Omega$ and $R_P = 17.8\ \Omega$. Values for energy gaps can be measured from the conductance data. We get 2Δ values of 0.76 meV and 1.38 meV which correspond to

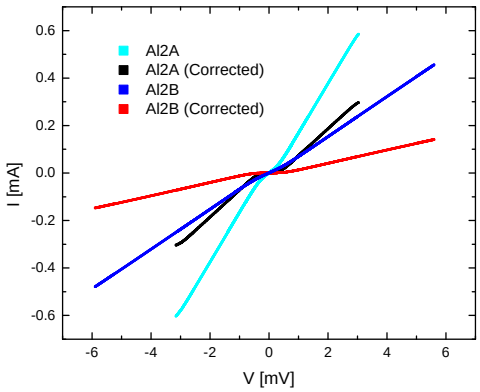

(a) IV on linear scale

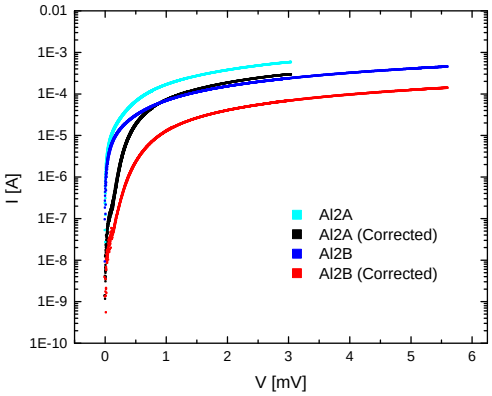

(b) IV on logarithmic scale

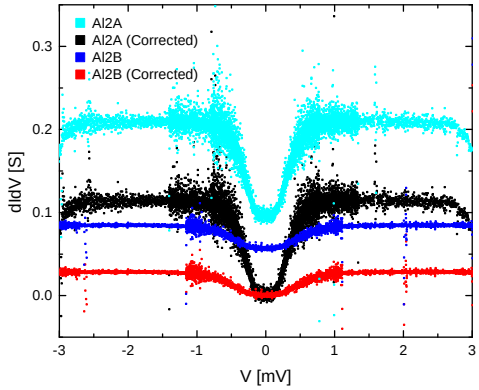

(c) Conductance calculated numerically from the IV

Figure 20: *Measured IV for Al2 samples. Also shows the data after the removal of parallel resistance (corrected data).*

single gap values of $\Delta = 0.38$ meV and $\Delta = 0.69$ meV.

Tunneling resistances of Al2A and Al2B are very different even though the process of sample fabrication is similar. The parallel resistances are of the same order of magnitude but still differ more from each other than the R_P values for Al1 samples. Also, both tunneling resistances are larger than would be expected from Al1 results. R_T is inversely proportional to the area of the junction which is $A_1 = 60\ \mu\text{m} \cdot 60\ \mu\text{m} = 3600 \mu m^2$ for Al1 samples

and $A_2 = 900\,\mu\text{m}^2$ for Al2. This gives a factor of $\frac{A_1}{A_2} = 4$ i.e. according to theory $R_{T2} \approx 4R_{T1}$, where 1 denotes to Al1 and 2 to Al2. However, R_T for Al2A is 14 times the R_T of Al1 samples ($0.65\,\Omega$) and 27 times for Al2B. This difference cannot be accounted for by the measurement error alone. In addition, the energy gaps of Al2 samples are higher than would be expected for aluminum. For Al2A it is 0.16 meV higher than expected Al gap (0.22 meV [27]) and for Al2B even 0.47 meV higher. This suggests that there is also a series resistance present in these samples in addition to the parallel resistance. Fig. 21 shows the proposed model for Al2 samples. Presence of a series resistance means that the bias voltage across the junction is smaller in reality than indicated by the measurement data.

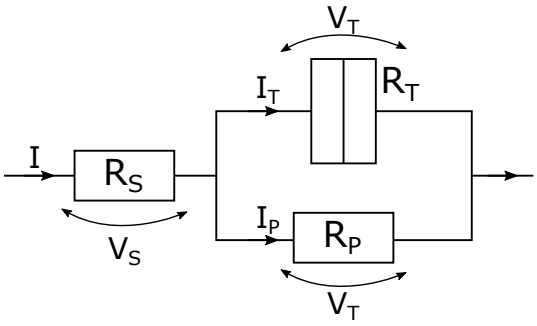

Figure 21: *Electrical model for samples containing parallel resistance R_P as well as series resistance R_S.*

4.2.2 $dI/dV(V)$ Measurements

Conductance was also measured directly for Al2A. Figure 22 shows the obtained dI/dV plot as a function of voltage. It can be seen that there is significantly less noise in the measured conductance compared to the calculated plot (Fig. 20c). That is expected, since the numerical differentiation used in the calculation does not usually produce clean data. Parameters of the junction obtained from the data are $R_P = 10.0\,\Omega$, $R_T = 11.6\,\Omega$ and $2\Delta = 0.76$ meV which corresponds to $\Delta = 0.38$ meV. The parallel resistance is very close to the value obtained from the IV, but there is a larger deviation

in tunneling resistance. Value for the energy gap Δ also suggests that the series resistance is present in Al2 samples.

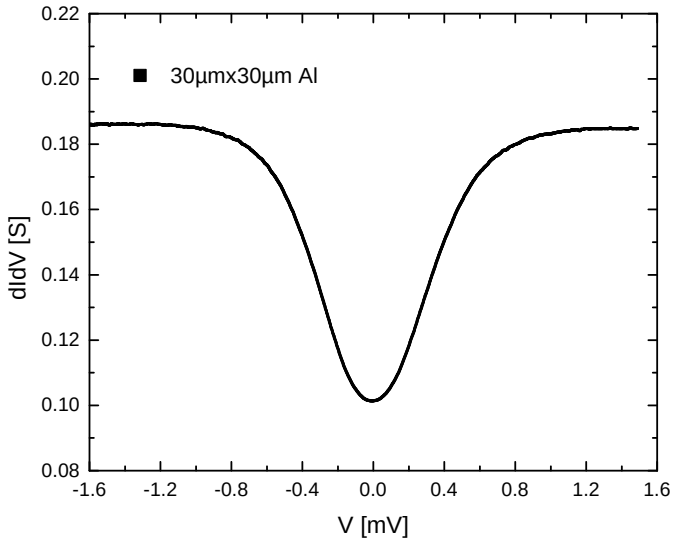

Figure 22: *Measured conductance of Al2A.*

4.2.3 Thermal Model Fit

Thermal model fitting was used for Al2A. The values used in the model were $n = 5$, $\Sigma = 1.8 \cdot 10^9$ (for Cu) and $V = 38\ \mu\text{m}^3$. Figure 23 shows the Al2A data with the thermal model fit. Figs. 23a and 23b show the IV plot on linear and logarithmic scale, respectively. Fig. 23c shows the conductance calculated from the IV data. Parameters for the fit are $R_T = 9.2\ \Omega$, $\Delta = 0.22$ meV, $T_{bath} = 0.3$ K, $\Gamma = 1 \cdot 10^{-2}$ and $\beta = 0.9$.

The fit corresponds well to the measured data at the energy gap i.e. at small bias voltages ($|V| < 0.2$ mV) but starts to deviate after that. As can be seen from Figs. 23a and 23b, the fit and the measured IV data are not in agreement above the gap. At least some of this can be accounted for by the series resistance present in the samples. The fit resembles the form of the conductance data somewhat well, and only deviates significantly at the

edges of the energy gap. The deviation is at least partly because the thermal model cannot account for all the heating present in the junction, as is the case for all the samples.

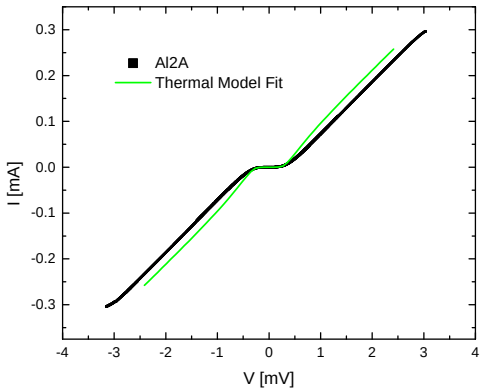

(a) IV on linear scale

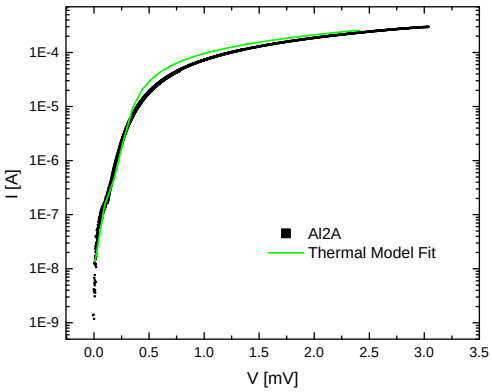

(b) IV on logarithmic scale

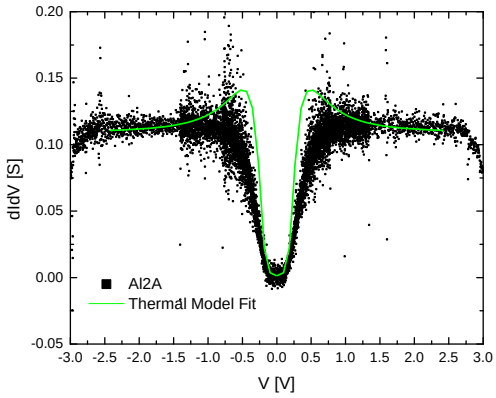

(c) Conductance calculated numerically from the IV

Figure 23: *Al2A IV data and the thermal model fit with parameters* $R_T = 9.2\ \Omega$, $\Delta = 0.22$ meV, $T_{bath} = 0.3$ K, $\Gamma = 1 \cdot 10^{-2}$ *and* $\beta = 0.9$.

The value for β is 0.9 for this sample which is little higher than for Al1 samples (0.7 and 0.8). This would indicate that 90% of the power removed from the normal metal is returned back. However, the presence of the parallel and the series resistance causes a large amount of heating which is not

accounted for in the thermal model.

4.2.4 Cooling Power

As was the case for Al1 samples, the cooling power of Al2 samples cannot either be measured because of the large self-heating present in these samples. It is still possible to estimate the cooling power of the samples by using typical fitting values for 30 μm x 30 μm Al SINIS junctions. Figure 24 shows the calculated cooling power $-P_N$ of the normal metal as a function of bias voltage. The values used for the calculation are $\Delta = 0.22$ meV and $R_T = 9.2\ \Omega$. The cooling power is calculated at three different temperatures ($0.2T_C$, $0.4T_C$ and $0.5T_C$), which correspond to temperatures 280 mK, 560 mK and 700 mK for aluminum. Also two different Dynes parameters are used: $\Gamma = 3 \cdot 10^{-2}$ and $\Gamma = 5 \cdot 10^{-2}$.

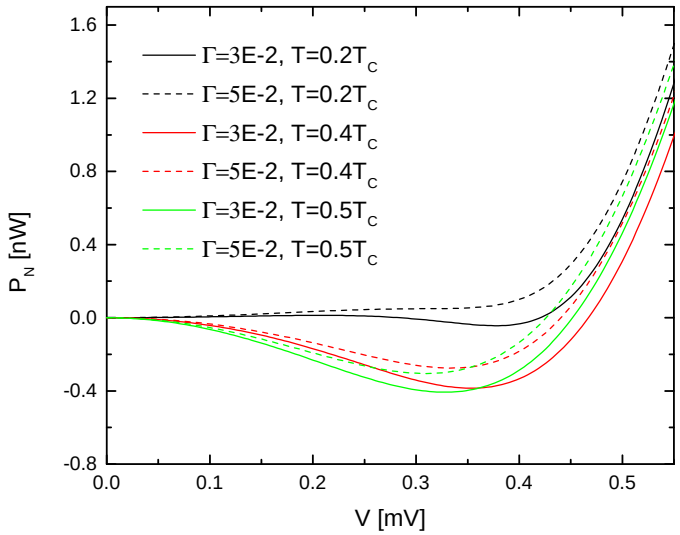

Figure 24: Calculated cooling power $-P_N$ of the normal metal for 30 μm x 30 μm Al SINIS tunnel junction at different temperatures. Typical values for the Dynes parameter are used.

Cooling is achieved when P_N is negative i.e. power is removed from the

normal metal. As can be seen from Fig. 24, there is cooling in all cases other than when $T = 0.2T_C$ and $\Gamma = 5 \cdot 10^{-2}$. For $T = 0.2T_C$ and $\Gamma = 3 \cdot 10^{-2}$, the cooling starts at $V = 0.28$ mV, and in other cases very close to $V = 0$. As was the case for Al1 samples, the maximum of cooling power is achieved at $0.5T_C$, whereas the largest range of cooling occurs at $0.4T_C$. The cooling power is larger with smaller values of the Dynes parameter in all temperatures. The maxima of the cooling power are 0.39 nW and 0.41 nW at $0.4T_C$ and 0.28 nW and 0.3 nW. Here the first value corresponds to the smaller Dynes parameter. The differences in the two maxima for different Dynes parameters are 20 pW at both temperatures respectively.

4.3 Nb Samples

4.3.1 $I(V)$ Measurements

IV measurements were conducted for two samples that had Nb as the superconducting electrode. They are named Nb1A and Nb1B. The obtained IV data is presented in Figure 25, where 25a and 25b are the linear and logarithmic representations. Fig. 25c shows the calculated conductance plots. The base temperature of the cryostat during the measurement is 105 mK - 132 mK for Nb1A and 108 mK - 143 mK for Nb1B.

The parallel resistance can be seen also in Nb1 samples. Values obtained from the IV and conductance data are $R_P = 11\ \Omega$, $R_T = 7.3\ \Omega$ for Nb1A and $R_P = 46\ \Omega$, $R_T = 5.1\ \Omega$ for Nb1B. Fig. 25 also shows the Nb1 sample data without the parallel resistance. Energy gap values are $2\Delta = 0.42$ meV and $2\Delta = 0.37$ meV respectively. These would correspond to single gap values $\Delta = 0.21$ meV and $\Delta = 0.19$ meV.

Tunneling resistances for both Nb1A and Nb1B are significantly larger than for Al1 samples which have the same junction area. Nb1A parallel resistance is higher than its R_T but still comparable which has been the trend in all samples. Nb1B parallel resistance is significantly higher, however, R_T is only 11% of R_P. The energy gaps of both samples do not correspond to the typical $\Delta = 1.5$ meV value for niobium. In fact, they are even somewhat small for aluminum. It is still reasonable to assume that the energy gap

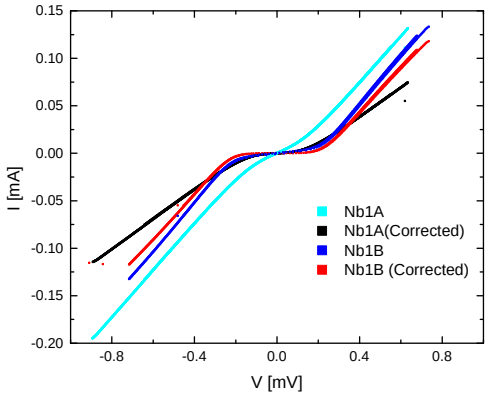

(a) IV on linear scale

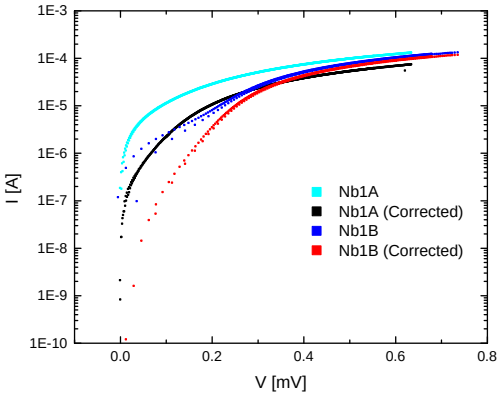

(b) IV on logarithmic scale

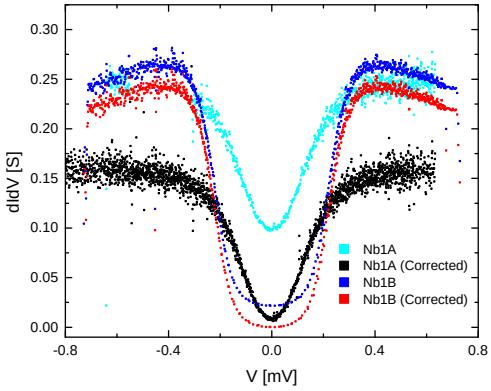

(c) Conductance calculated numerically from the IV

Figure 25: *Measured IV for Nb1 samples. Also shows the data after the removal of parallel resistance (corrected data).*

comes only from aluminum that is evaporated on top of Nb to create the tunneling barrier, since Nb gap would be an order of magnitude higher at these temperatures. The energy gap of Nb1B is much better defined than of Nb1A as can be seen from Fig. 25c, even though the base temperatures are very similar. This is in agreement with the large parallel resistance since there is now less heating due to smaller current through the path with R_P.

4.3.2 $dI/dV(V)$ Measurements

Conductance of Nb1B was measured also directly. The dI/dV plot is shown in Figure 26. The junction parameters obtained from the data are $R_P = 46\ \Omega$, $R_T = 5.4\ \Omega$ and the energy gap 0.37 meV corresponding to a single gap $\Delta = 0.19$ meV. All these values correspond really well to the IV measurement of the same sample.

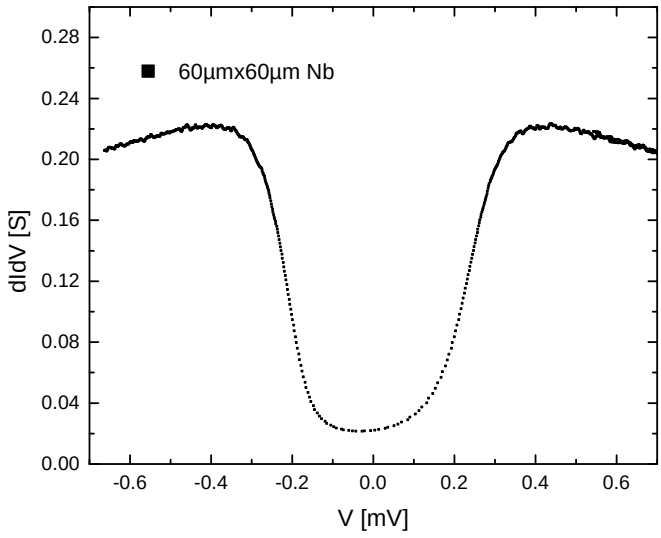

Figure 26: *Measured conductance of Nb1B.*

4.3.3 Thermal Model Fit

Fitting was done to Nb1A data using the thermal model, the data and fit are shown in Figure 27. The values used in the model were $n = 5$, $\Sigma = 1.8 \cdot 10^9$ (for Cu) and $V = 180\ \mu\text{m}^3$. The parameters of the resulting fit are $R_T = 7.3\ \Omega$, $\Delta = 0.30$ meV, $T_{bath} = 0.17$ K, $\Gamma = 7 \cdot 10^{-2}$ and $\beta = 4$. The fit follows the IV data quite well having only small deviations at low bias voltages. Conductance plot (Fig. 25c) reveals that the fit is not ideal in the energy gap but becomes better as the bias gets larger.

R_T and T_{bath} are close to measured values, even though T_{bath} is higher than the base temperature of the cryostat but still being only slightly elevated. The energy gap for Nb1A fit would have been only 0.15 meV if a fit for SINIS junction was used. The thermal model uses $\Delta(T = 0)$ as the fitting parameter for energy gap and the value used for Nb1A is too small for even $Al/AlO_x/Cu$ SINIS junction. For that reason the single NIS fit was used. The data suggests that one of the junctions is not working and is just short circuited resulting to only a single energy gap Δ. The measured IV data also supports this theory, but it did not give enough evidence without the fit because large heating can also affect the energy gap. This single NIS theory would also change the energy gap value obtained from the IV data to $\Delta = 0.42$ meV. This is larger than the value used in the fit (0.30 meV) but both of these are larger than Al gap. Though still significantly smaller than the pure Nb gap, this most likely means that the Al gap is increased by the proximity effect of the Nb layer [8].

The Dynes parameter is high in this sample, but it is still similar to Al1 samples that have the same junction area. This higher value can be caused by the presence of niobium in the sample because Nb typically has a higher Dynes parameter than Al [27]. β used in the fit is significantly larger than in any other sample. Because β is a fraction of the power returning back to the normal metal from the total power, it would not be physically meaningful to use values larger than 1. However, it was not possible to get any kind of fit without using such high values. There is heating due to the parallel resistance in the sample which is not taken into account directly in the thermal model, so this could cause a heating power larger than the power removed from the normal metal.

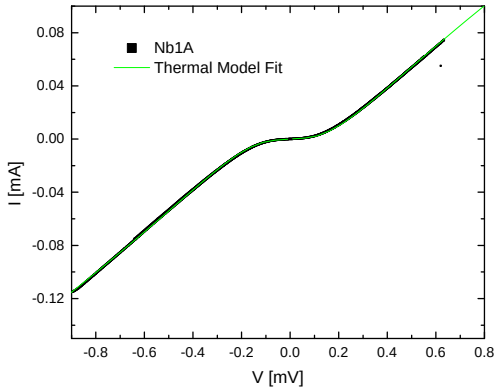

(a) IV on linear scale

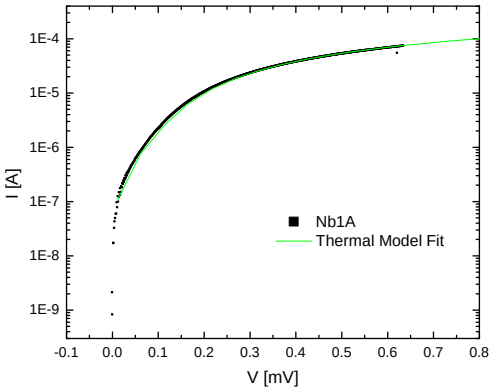

(b) IV on logarithmic scale

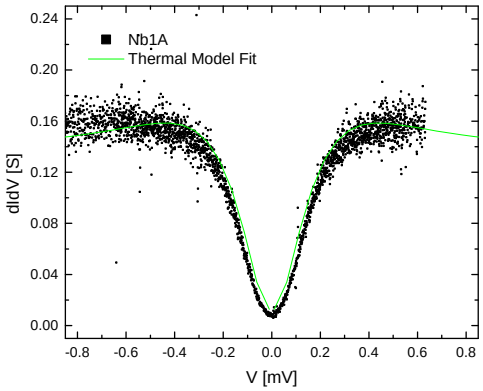

(c) Conductance calculated numerically from the IV

Figure 27: *Nb1A IV data and the thermal model fit with parameters* $R_T = 7.3\ \Omega$, $\Delta = 0.30$ meV, $T_{bath} = 0.17$ K, $\Gamma = 7 \cdot 10^{-2}$ *and* $\beta = 4$.

5 Conclusions and Outlook

Measurement data of Al/AlO_x/Cu junctions show the principle characteristics of NIS tunnel junctions. There is still significant deviation from that behavior in both 60 μm x 60 μm Al1 and 30 μm x 30 μm Al2 samples. Both types of samples are likely to contain a parallel resistance which would account for some of the differences in the samples. Al2 samples have much larger deviation from ideal situation than Al1. There seems to be an additional series resistance in these samples. All these extra resistances cause significant heating of the junctions at nonzero biases so all of it could not be accounted for even with the thermal fitting model.

Data for Nb/Al/AlO_x/Cu also resemble the ideal behavior but the energy gap is very close to the aluminum gap. This suggests that the proximity effect of the Nb layer is not strong enough, and thus Nb is not contributing to the S layer of the junction.

Results suggest that it is possible to fabricate large area tunnel junctions that could be used in cooling in the future. However, in order to do so, the origin of the parallel and series resistance must be identified properly. After that, both of these should be eliminated from the samples, e.g. by modifying the sample geometry to get rid of the extra heating effects, which prevents the electronic cooling with the NIS junctions. A possible origin for the heating could be a direct N-S (normal metal-superconductor) contact, i.e. there is no tunneling barrier (I) between the two layers in all places. Also, there can be pinholes in the insulating SiO_2 layer between the two NIS junctions. One possibility to improve the structure, is to use a different normal metal, such as gold, instead of copper, in the future. In addition, more study is needed for large area junctions with niobium as the superconductor.

References

[1] I. Giaever. Energy gap in superconductors measured by electron tunneling. *Phys. Rev. Lett.*, 5(4), 1960.

[2] J. C. Fisher and I. Giaever. Tunneling through thin insulating layers. *Journal of Applied Physics*, 32(172), 1961.

[3] K. E. Gray and H. W. Willemsen. Inhomogeneous state of superconductors by intense tunnel injection of quasiparticles. *Journal of Low Temperature Physics*, 31(5-6), 1978.

[4] M. Nahum, T. M. Eiles, and J. M. Martinis. Electronic microrefrigerator based on a normal-insulator-superconductor tunnel junction. *Appl. Phys. Lett.*, 64(24), 1994.

[5] M. M. Leivo, J. P. Pekola, and D. V. Averin. Efficient peltier refrigeration by a pair of normal metal/insulator/superconductor junctions. *Appl. Phys. Lett.*, 68(14), 1996.

[6] A. M. Clark, A. Williams, S. T. Ruggiero, M. L. van den Berg, and J. N. Ullom. Practical electron-tunneling refrigerator. *Appl. Phys. Lett.*, 84(625), 2004.

[7] J. P. Castle, M. F. Cunningham, B. Neuhauser, S. Golwala, F. P. Lipschultz, A. Barootkoob, O. B. Drury, M. Frank, J. Jochum, S. E. Labov, C. A. Mears, B. Sadoulet, A. Slepoy, and D. A. Yale. Preparation and characterization of $Al/Al_2O_3/Cu$ tunnel junctions microfabricated with a full wafer process. *Czechoslovak Journal of Physics*, 46(5), 1996.

[8] M. R. Nevala, S. Chaudhuri, J. Halkosaari, J. T. Karvonen, and I. J. Maasilta. Sub-micron normal-metal/insulator/superconductor tunnel junction thermometer and cooler using Nb. *Appl. Phys. Lett.*, 101(112601), 2012.

[9] S. Chaudhuri, M. R. Nevala, and I. J. Maasilta. Niobium nitride-based normal metal-insulator-superconductor tunnel junction microthermometer. *Appl. Phys. Lett.*, 102(132601), 2013.

[10] J. T. Muhonen, M. Meschke, and J. P. Pekola. Micrometer-scale refrigerators. *Rep. Prog. Phys.*, 75(046501), 2012.

[11] C. K. Stahle, D. McCammon, and K. D. Irwin. Quantum calorimetry. *Physics Today*, 52(8), 1999.

[12] H. Q. Nguyen, M. Meschke, J. P. Pekola, and H. Courtois. Sub-50 mk electronic cooling with large-area superconducting tunnel junctions. *Phys. Rev. Applied*, 2(054001), 2014.

[13] P. J. Lowell, G. C. O'Neil, J. M. Underwood, and J. N. Ullom. Macroscale refrigeration by nanoscale electron transport. *Appl. Phys. Lett.*, 102(082601), 2013.

[14] M. Tinkham. *Introduction to Superconductivity.* McGraw-Hill, New York, 2nd edition, 1996.

[15] C. Kittel. *Introduction to Solid State Physics.* John Wiley & Sons, 8th edition, 2005.

[16] J. Bardeen, L. N. Cooper, and J. R. Schrieffer. Theory of superconductivity. *Phys. Rev.*, 108(5), 1957.

[17] S. R. Elliott. *The Physics and Chemistry of Solids.* John Wiley & Sons, 1998.

[18] R. C. Dynes, J. P. Garno, G. B. Hertel, and T. P. Orlando. Tunneling study of superconductivity near the metal-insulator transition. *Phys. Rev. Lett.*, 53(2437), 1984.

[19] G. C. O'Neil. *Improving NIS Tunnel Junction Refrigerators: Modeling, Materials, and Traps.* PhD thesis, University of Colorado, 2011.

[20] J. P. Pekola, V. F. Maisi, S. Kafanov, N. Chekurov, A. Kemppinen, Y. A. Pashkin, O. P. Saira, M. Möttönen, and J. S. Tsai. Environment-assisted tunneling as an origin of the Dynes density of states. *Phys. Rev. Lett.*, 105(026803), 2010.

[21] D. J. Griffiths. *Introduction to Quantum Mechanics.* Pearson Prentice Hall, 2nd edition, 2004.

[22] C. Poole. *Superconductivity.* Elsevier, 2nd edition, 2007.

[23] P. Koppinen. *Applications of Tunnel Junctions in Low-Dimensional Nanostructures.* PhD thesis, University of Jyväskylä, 2009.

[24] S. Chaudhuri and I. J. Maasilta. Cooling, conductance, and thermometric performance of nonideal normal metal-superconductor tunnel junction pairs. *Phys. Rev. B*, 85(014519), 2012.

[25] F. Giazotto, T. T. Heikkilä, A. Luukanen, A. M. Savin, and J. P. Pekola. Opportunities for mesoscopics in thermometry and refrigeration: Physics and applications. *Reviews of Modern Physics*, 78(1), 2006.

[26] M. M. Leivo. *On-Chip Cooling by Quasiparticle Tunneling Below 1 Kelvin.* PhD thesis, University of Jyväskylä, 1999.

[27] M. R. Nevala. *Development of Niobium-Based Superconducting Junctions.* PhD thesis, University of Jyväskylä, 2012.

[28] S. Franssila. *Introduction to Microfabrication.* John Wiley & Sons, 2nd edition, 2010.

[29] F. Pobell. *Matter and Methods at Low Temperatures.* Springer, 3rd edition, 2010.

[30] J. M. Rowell, M. Gurvitch, and J. Geerk. Modification of tunneling barriers on Nb by a few monolayers of Al. *Phys. Rev. B*, 24(4), 1981.

[31] A. Sergeev and V. Mitin. Electron-phonon interaction in disordered conductors: Static and vibrating scattering potentials. *Phys. Rev. B*, 61(6041), 2000.